Processing and Properties of Zirconia-CNT Composites

A thesis submitted to Universitat Politècnica de Catalunya and Luleå University of Technology for the double degree of Doctor of Philosophy by

Latifa Melk

Dept. of Materials Science and Metallurgical Engineering at UPC
Dept. of Engineering Sciences and Mathematics at LTU

Thesis directors: Prof. Marc Anglada and Ass. Prof. Marta-Lena Antti

UNIVERSITAT POLITÈCNICA DE CATALUNYA

May 2016

"Nothing in life is to be feared, it is only to be understood. Now is the time to understand more, so that we may fear less."

~Marie Curie~

ABSTRACT

In the last decades there has been growing interest in developing ceramic materials with high fracture toughness (K_{Ic}) and strength for structural applications. In the specific case of 3 mol % yttria-doped tetragonal zirconia (3Y-TZP), K_{Ic} can be increased by promoting phase transformation from tetragonal (*t*) to monoclinic (*m*) phase in front of a propagating crack tip referred to as transformation toughening. However, the stronger the tendency for stress induced transformation, the higher the risk for premature spontaneous *t-m* transformation in humid atmosphere. This phenomenon, which is referred to as ageing, hydrothermal degradation or low temperature degradation (LTD) induces microcracking and loss of strength and limits the use of 3Y-TZP. The resistance to LTD can be increased by reducing the grain size into the nanoscale by using Spark Plasma Sintering (SPS). However, the reduction of grain size may reduce *t-m* phase transformation in front of the crack tip and therefore fracture toughness may decrease. One way to enhance K_{Ic} is the incorporation of a second phase as a toughening mechanism into zirconia matrix. In the present study, Multi-Walled Carbon Nanotubes (MWCNTs) were used to reinforce zirconia matrix.

A novel method was developed in this project in order to measure the "true" fracture toughness of small cracks of 3Y-TZP/CNT composites. The method is based on producing a very sharp notch using Ultra-short Laser Ablation (UPLA). The same method was also applied to a high toughness zirconia ceramic 12Ce-ZrO_2 with 300 nm grain size, which has much higher plateau fracture toughness than SPSed 3Y-TZP with 177 nm grain size. Moreover, the wear behaviour of zirconia/CNT composite was investigated by studying the effect of CNTs on the friction coefficient and the wear rate of the composites. The wear behaviour was investigated with scratch tests and reciprocating sliding. The machinability of zirconia/CNTs using Electrical Discharge Machining (EDM) was evaluated by studying the electrical conductivity, the thermal conductivity and the damage produced after machining. Besides that, the influence of grinding, thermal etching after grinding, and annealing of SPS zirconia with different grain sizes were studied.

It has been found that by inducing a very sharp shallow notch using UPLA, the "true" K_{Ic} of SPSed 3Y-TZP and 3Y-TZP/CNT composites for small cracks is low and independent of the added CNT amount. On the contrary, Vickers indentation K_{Ic} is higher and increases with CNT content, which is attributed to the larger crack sizes studied in indentation and to an increase in the resistance to cracking under sharp

contact loading induced by the presence of CNT. Therefore, indentation K_{Ic} is not an appropriate method for analysing the influence of MWCNT on "true" fracture toughness. Moreover, only 10 % of difference in strength was found in 12Ce-ZrO_2 and 3Y-TZP using UPLA method indicating that the "true" K_{Ic} of both materials is almost similar. Thus, the beneficial effect of higher indentation K_{Ic} in 12Ce-ZrO_2 reported in literature has a very small effect on the "true" K_{Ic} that determines the strength of unshielded small cracks.

The incorporation of CNTs into zirconia matrix increases the friction coefficient and drastically decreases the wear rate when the amount of CNT reaches the percolation value (2 wt % CNT) under relatively low loads. However, during scratch test and under high loads, the composites develop chipping and brittle fracture.

The addition of CNTs strongly enhances the electrical conductivity of the composite and induces slight changes in the thermal conductivity which results in successful EDM machining of the composites with 1 wt % and 2 wt % CNT. The material removal mechanisms in the composites are melting/evaporation and spalling.

The thermal etching of ground SPS zirconia at 1100 °C for 1 hour in air induces a surface nanograin layer with crystallized grains of about 60 nm sizes and a thickness of less than few hundred nanometers, which is independent of the original grain size of the bulk material. If thermal etching is carried out at much higher temperature, 1575 °C for 1 hour, ground and polished zirconia reaches similar grain size.

ACKNOWLEDGMENTS

Although it is just my name on the cover, many people have contributed to the research in their own particular way and without them this project would never have been possible.

First, I would like to express my gratitude to my principal supervisor Prof. Marc Anglada at UPC, in Spain, who has taught me a lot in Science and also in life. You allowed me to develop myself as a researcher in the best possible way.

Then, I would like to acknowledge my second supervisor Ass. Prof. Marta-Lena Antti at LTU in Sweden. I greatly appreciate the freedom you have always given me to find my own path and the support you offered me when needed.

I am grateful to the kind people at the division of Materials Science at LTU. I started with you when I was an undergraduate student and I grew up among all of you. Thank you wonderful people: Ragnar Tegman, Esa Vuorinen, Johnny Grahn and Lars Frisk for the heart-warming support.

I´m thankful to the people I worked with in the department of Materials Science and Metallurgical Engineering at UPC. Your help and support made me realise that I am only a beginner in this exciting profession.

I also would like to thank all my colleagues at both UPC and LTU and my friends from all over the world for your advices, constant enthusiasm and encouragement.

Last but not least, I would like to thank my family for their encouragement, my Mom and Dad, my sister Sara and my brothers Zakaria and Yahya. I undoubtedly could not have done this without you.

A special thanks to my partner Omar Benjelloun, you were always there for me with your quiet patience and unwavering love.

تحية خالصة للعائلتين مِلك و الرسولي
"لطيفة"

APPENDED PAPERS

Paper I

L. Melk, J.J. Roa Rovira, M-L. Antti, M. Anglada, Coefficient of friction and wear resistance of zirconia–MWCNTs composites, Ceram. Int. 41 (2014) 459-468.

Paper II

L. Melk, J.J. Roa Rovira, F. García-Marro, M.-L. Antti, B. Milsom, M.J. Reece, M. Anglada, Nanoindentation and fracture toughness of nanostructured zirconia/multi-walled carbon nanotube composites, Ceram. Int. 41 (2015) 2453-2461.

Paper III

L. Melk, M. Turon-Vinas, J.J. Roa, M.L. Antti, M. Anglada, The influence of unshielded small cracks in the fracture toughness of yttria and of ceria stabilised zirconia, J. Eur. Ceram. Soc. 36 (2016) 147–153.

Paper IV

L. Melk, M-L. Antti, M. Anglada, Material removal mechanisms by EDM of zirconia reinforced MWCNT nanocomposites, Ceram. Int. 42 (2016) 5792-5801.

Paper V

L. Melk, J. Mouzon, F. Akhtar, M. Turon-Vinas, M-L. Antti, M. Anglada, Surface microstructural changes of Spark Plasma Sintered Zirconia after grinding and annealing, to be submitted.

Conference contributions not included in the thesis

L. Melk, F.G. Marro, A. Mestra, E. Jimenez-Piqué, and M. Anglada, *Effect of MWCNT addition on the friction coefficient and electrical properties of 3Y-TZP, Poster presentation at the 13th European Inter-Regional Conference on Ceramics. Barcelona, Spain, September 2012.*

L. Melk, J. J. R. Rovira, F. G. Marro, M. Anglada, *Mechanical and Electrical properties of 3Y-TZP/CNT composites, Abstract at the 7th EEIGM conference. Luleå, Sweden, March 2013.*

L. Melk. J. J. Rovira, F. G-Marro, M.L Antti, B. Milsom, M. J. Reece, and M. Anglada, *Friction and Scratch Damage in 3Y-TZP/MWCNT composites, Oral presentation at the 13th International Conference of the European Ceramic society. Limoges, France, June 2013.*

L. Melk, J. J. R. Rovira, M-L Antti, M. Anglada, *Coefficient of friction and wear resistance of 3Y-TZP/CNT nanocomposites, Oral presentation at the 14th European Inter-Regional Conference on Ceramics. Stuttgart, Germany, September 2014.*

L. Melk, M-L Antti, M. Anglada, the effect of SPS temperature on the mechanical properties of zirconia/CNTs composites, *Oral presentation at 8th EEIGM Conference. Valencia, Spain, June 2015.*

M Turon-Vinas, L. Melk, J.J. Roa, M-L Antti, M. Anglada, *Determination of fracture toughness from notches induced by ultra-short pulsed laser ablation, Abstract at European Ceramic Society conference. Toledo, Spain, June 2015.*

L. Melk, M-L Antti, M. Anglada, *Mechanical and tribological properties of spark plasma sintered 3Y-TZP and 3Y-TZP reinforced MWCNTs composites, Oral presentation at European Congress and Exhibition on Advanced Materials and Processes. Warsaw, Poland, September 2015.*

CONTENTS

PART I

Part I

CHAPTER 1

Introduction

1.1 Zirconia ceramics

1.1.1 Zirconia structure

Zirconia is polymorphic of nature. It displays three different crystallographic structures depending on temperature. It exhibits a monolithic structure (*m*) from room temperature up to 1170 °C, a tetragonal structure (*t*) at intermediate temperatures (1170-2370 °C) and a cubic structure (*c*) when the temperature is above 2370 °C, see Fig. 1.1.

The phase transformation from *t* to *m* is associated with a volume expansion of approximately 0.05 which induces microcracking. The *t-m* transformation starts at ≈950 °C (M_s) on cooling in pure zirconia and is reversible on heating around 1150 °C [1]. The incorporation of some oxide dopants such as magnesium oxide (MgO), calcium oxide (CaO), cerium oxide (CeO_2) and yttrium oxide (Y_2O_3) can suppress the phase transformation and stabilize zirconia in tetragonal form or even in cubic form. The major types of stabilized zirconia are formed depending on the final microstructure achieved: Fully Stabilized Zirconia (FSZ) is formed with full cubic structure. Partially Stabilized Zirconia (PSZ) contains cubic zirconia as the major phase while monolithic and tetragonal zirconia precipitate as minor phases. Tetragonal Zirconia Polycrystals (TZP) consists of tetragonal phase retained in a metastable state when cooled to room temperature.

Y_2O_3 and CeO_2 are the most promising stabilizers. They retain the tetragonal phase at room temperature in the form of TZP where the microstructure consists of equiaxed fine-grains [2]. The oxygen overcrowding around the small zirconium Zr^{4+} cations was shown to be responsible for the poor stability of tetragonal zirconia. Therefore, the use of oversized trivalent cation (Y^{3+}) to stabilize tetragonal zirconia is more efficient than undersized trivalent cations [3,4].

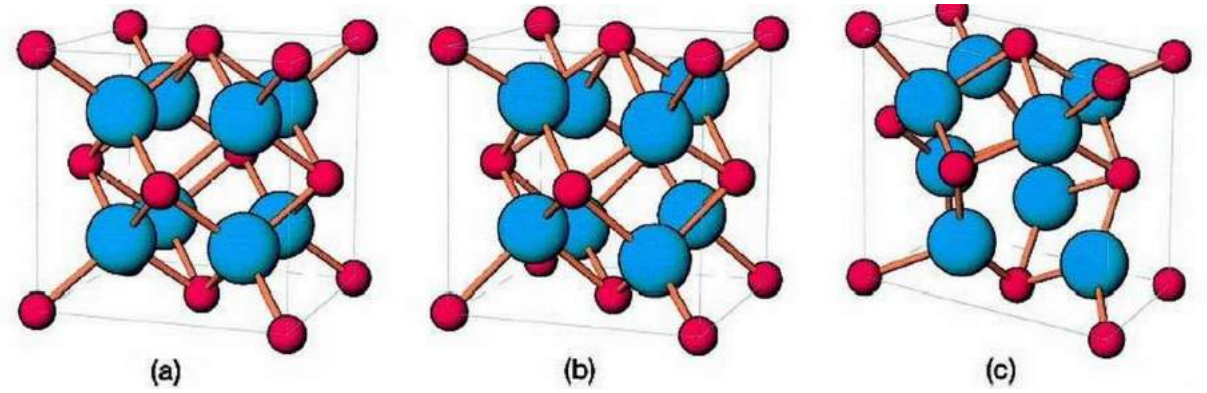

Fig. 1.1 Schematics of the three polymorphs of ZrO_2 and the corresponding space groups: (a) cubic (b) tetragonal and (c) monoclinic [4].

1.1.2 Transformation from tetragonal (t) to monoclinic (m)

The transformation from *t* to *m* in zirconia is martensitic of nature. Although martensitic transformation is originally associated with transformation in quenched steels, it occurs as well in minerals and ceramics. A crystallographic correspondence of martensitic transformation exists between the parent (tetragonal) and the product (monoclinic) phase, described by habit planes and directions (shape strain) as shown in Fig. 1.2. The martensitic transformation is a change in crystal structure in the solid state through a diffusionless process. It is athermal and involves the simultaneous, cooperative movement of atoms over distances less than an interatomic distance which results in microscopic changes of shape of the transformed regions. This change in shape is associated with transformation toughening [5].

The thermodynamics of the *t-m* transformation (martensitic) in zirconia was first described by Lange [6] considering the ideal configuration of a spherical tetragonal particle in a matrix. The change of the total free energy (ΔG_{t-m}) associated to the transformation is given by equation (1.1):

$$\Delta G_{t-m} = \Delta G_c + \Delta U_{SE} + \Delta U_S \qquad (1.1)$$

where ΔG_c (<0 at temperatures below the equilibrium M_s) is the difference in chemical free energy between tetragonal and monoclinic phases and it depends on temperature and composition. ΔU_{SE} (>0) is the change in elastic strain energy associated to the transformation of particles and it depends on the modulus of the surrounding matrix, the size and shape of the particle and the presence of external stresses. Finally, the term ΔU_S (>0) refers to the change in the energy associated to the formation of new interfaces between the transformed particle and the matrix. In the case of ΔG_{t-m}<0 the tetragonal phase is unstable and a transformation to monoclinic may occur. If ΔG_{t-m} >0, the tetragonal phase retains in the particle. A decrease in $|\Delta G_c|$ and an increase in

ΔU_{SE} followed by the addition of some oxides such as Y_2O_3 in Y-TZP, induce a decrease in the driving force of the *t-m* transformation and its temperature [3]. The transformation from (*t*) to (*m*) in zirconia is the source of enhanced toughness.

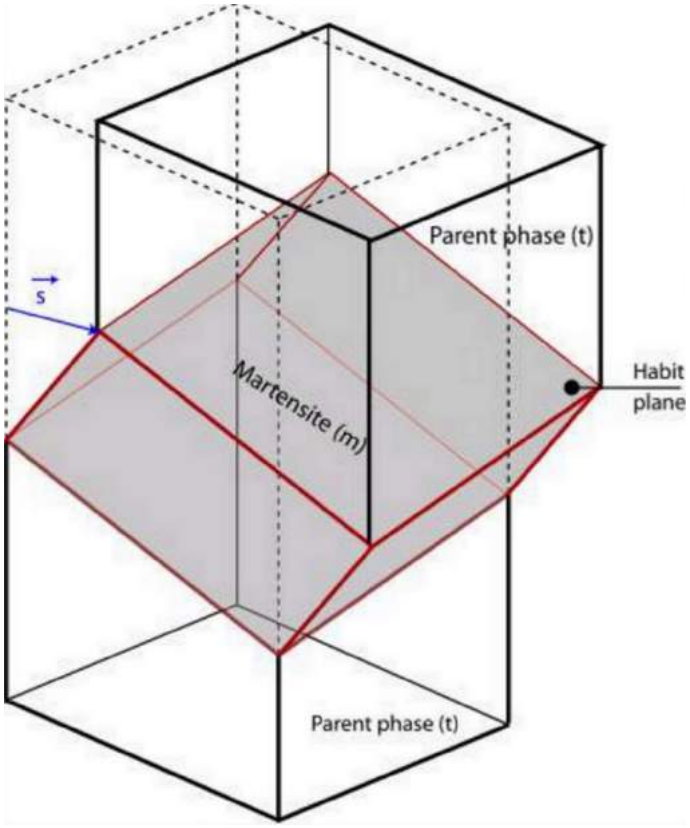

Fig.1.2 Schematic illustration of the crystallographic correspondences between the tetragonal (parent) and the monoclinic (product) phases during the martensitic t-m transformation.

1.1.3 The mechanism of toughening in zirconia

Transformation toughening

The two material classes better known to exhibit transformation toughening are transformation-induced plasticity (TRIP) steels and zirconia based ceramics [5].
Series of theoretical models have been developed to explain transformation toughening phenomena and they all agree on the development of a transformed "process" zone associated with an advancing crack where a transformation of the metastable (*t*) phase takes place at the crack tip [4], see Fig.1.3.
The tensile stresses generated induce a phase transformation from *t* to *m* around the crack tip and induce an increase in volume. The large volume generates compressive stresses around the crack and stops further crack propagation [3,4,7].

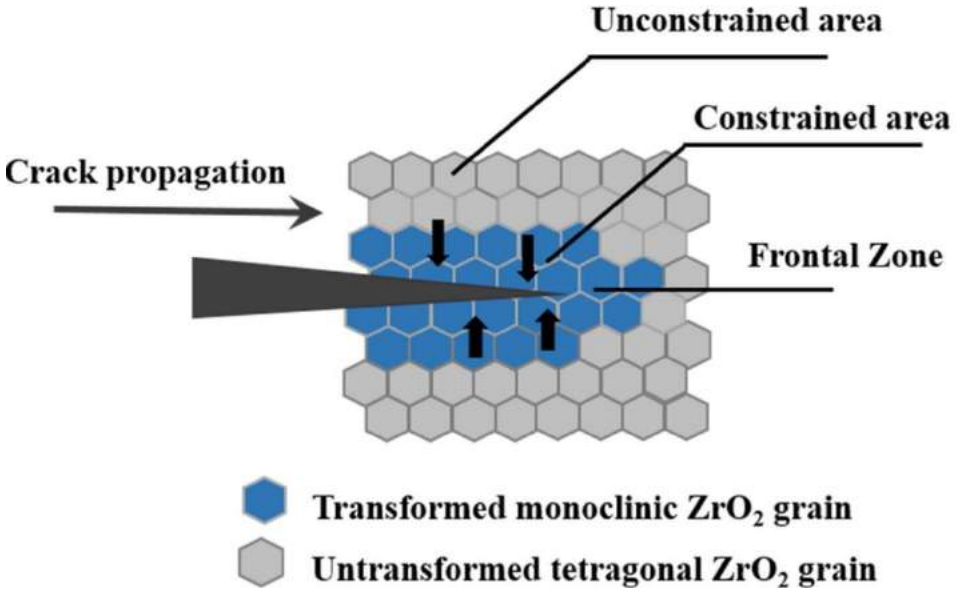

Fig. 1.3 Illustration of transformation toughening in front of a propagation crack [8].

In 1980, McMeeking and Evans [7] developed a model of phase transformation toughening using linear elastic fracture mechanics. The model is based on the fact that the stress induced transformation toughening leads to a shielding, K_{Ish} of the applied stress intensity factor K_I which means that real stress intensity factor at the crack tip K_{Itip} is lower than that applied by external forces according to the following relation:

$$K_{Itip} = K_I - K_{Ish} \tag{1.2}$$

where K_{Itip} is the stress intensity factor at the crack tip, K_I is the applied stress intensity factor and K_{Ish} is the shielding factor.
Previous studies show that the higher the applied stress intensity factor, the larger the transformation zone and the larger shielding effect as shown in the following equations (1.3) and (1.4):

$$K_{Ish} = C_{sh} K_I \tag{1.3}$$

$$C_{sh} = \frac{0.214 E V_f e^T (1+\nu)}{(1-\nu)\sigma_m^c}\left(\frac{\sqrt{3}}{12\pi}\right) \tag{1.4}$$

where E is the elastic modulus, V_f is the volume fraction of the transformable particles, e^T is the dilatational strain associated with the transformation, ν is the Poisson ratio and σ_m^c is the critical stress leading to phase transformation.

The toughness of zirconia depends directly on the critical local stress leading to transformation σ_m^c. A material with low V_f and/or e^T and a high σ_m^c will have low values of C_{sh} so that the contribution of transformation to shielding will be small ($C_s << 1$). On the contrary, with high V_f and/or e^T and low σ_m^c , a large C_{sh} (>>1) results in strong transformation, as far as the transformation is localised in front of the crack. The local stress transformation depends on the magnitude of the temperature of undercooling below the T_0 (t/m) temperature. The larger the undercooling below T_0 (t/m) the lower critical stress for stress assisted phase transformation, then the larger the transformation toughening [3,4].

Ferro-elastic toughening

Besides phase transformation toughening, there is another mechanism of toughening referred to as induced ferro-elastic domain switching which also enhance the toughness of zirconia based ceramics. It is referred to as ferro-elastic toughening. In 1998, Virkar and Matsuimoto [9] reported for the first time, high values of toughness related to the ferro-elastic domain switching. The mechanism of the ferro-elastic toughening involves switching or alignment of the *c*-axis of the *t*-phase along the maximum stress axis, which induces a shape change of a pure shear type. Ferro-elastic toughening is possible in tetragonal zirconia produced by cooling from the cubic phase by a composition invariant displacive reaction. It can also occur when a direct deposition of tetragonal-prime zirconia takes place by sputtering or electron-beam deposition for example [3].

1.1.4 R-curve behaviour

R-curve, or crack resistance, is an increasing resistance of the material to crack growth under stress intensity factors higher than the crack lattice intrinsic fracture toughness. In general, R-curve behaviour is displayed by any material that exhibits nonlinearity in its stress-strain behaviour and experiences a crack-stabilizing effect [10]. The R-curve behaviour is more dominant for larger cracks because the effect of toughening mechanisms at the crack tip increases with the increase in crack size [11]. R-curve behaviour in ceramics is a result of extrinsic toughening mechanisms that are operating in the wake of a propagating crack, hence, an R-curve is referred as toughness-curve (t-curve) [12]. The increasing in toughness or R-curve for some ceramics is shown in Fig.1.4. Mg-PSZ exhibits a high crack resistance compared to Y-TZP which hardly has R-curve. The typical R-curve of Mg-PSZ is a result of transformation toughening in addition to crack deflection which both are crack shielding extrinsic toughening effects as reported by Hoffman [10].

A study by Eichler et al. [13] showed that the R-curve depends on the grain size and the testing environment. In the case of 2Y-TZP with grain size of 300 nm, the R-curve reaches values up to 5.4 MPa√m in ambient air and 6.7 MPa√m in vacuum.

Moreover, the authors reported no rising crack resistance with increasing crack length in air because of the smaller transformation zone. Gupta et al.[14] reported a fracture toughness of 5.7 for a grain size of 250 nm which is in line with the results reported before [13]. However, Fargas et al. [15] observed a small increase in plateau toughness in air from 3.9 to 4.3 MPa√m in 2.5Y-TZP with grain size of 300 nm.
R-curves have been studied for many materials since the first detection of a rising crack growth resistance curve by Hübner and Jillek [16] in 1977. Then, most of the work on R-curves has been conducted on specimens with macrocracks and indentation cracks.
Munz [17], in his review about "what we can learn from R-curve measurements" reported that the principal R-curve behaviour of a material can be measured with macrocracks. However, a quantitative prediction of the R-curve for natural flaws is not possible from measurements of specimens with macrocracks or with indentation cracks. Moreover, the investigation of materials with a rising R-curve results in increase in strength compared to a material with the same lattice intrinsic fracture toughness and a flat R-curve.

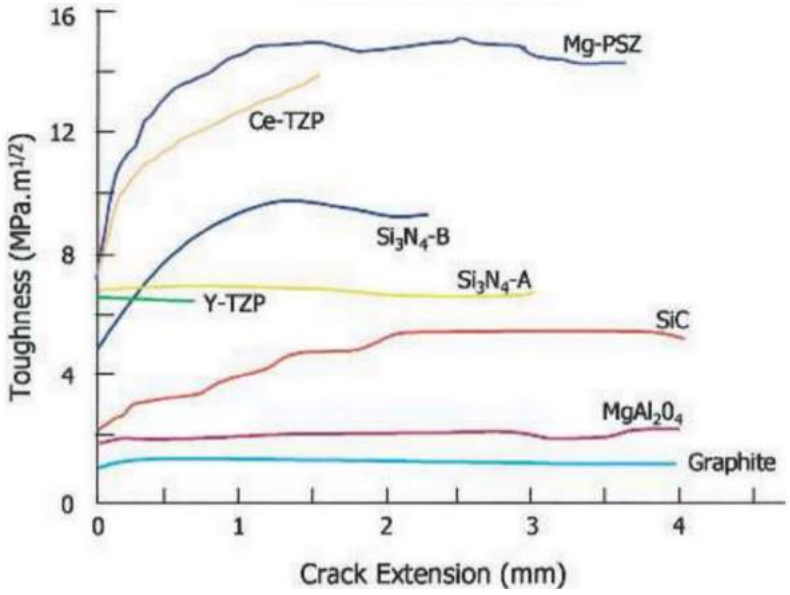

Fig. 1.4 R-curves for some ceramic materials obtained from measurements of long cracks in compact tension samples [4].

1.1.5 Low thermal degradation of zirconia

Low thermal degradation (LTD), referred to as hydrothermal degradation or aging, was first reported by Kobayashi et al. [18] in 1981 who discovered that zirconia samples could suffer from slow *t-m* transformation at the surface in humid atmosphere at 250 °C resulting in microcracking and loss of strength. Many investigations have been

conducted to understand the LTD phenomena since its discovery, but it is still under debate. LTD was always considered important only at temperatures above human body or room temperature (37 °C) until 2001 when several of hundreds of hip prosthesis failed in a short time due to aging of zirconia femoral heads implanted in patients. This catastrophe limited the use of zirconia in medical applications and more deep investigations were needed to understand LTD of zirconia [1].
During LTD the degradation of properties is associated with the transformation from tetragonal to monoclinic phase. The reversible transformation (*m–t*) can occur, and then a total strength recovery is achieved, but only when aged specimens are annealed at high temperatures [19]. Yoshimura summarized experimental observations of LTD on zirconia as follows:

- LTD is accelerated at temperatures of 200-300 °C and it is time dependent.
- LTD is due to *t-m* transformation accompanied by micro- and macro-cracks.
- The transformation progresses from the surface to the interior of the sample.
- The transformation is enhanced by water or water vapour.
- A decrease of the grain size and increase of stabilizer retards the transformation.

The mechanism of LTD as reported in the work of Sato et al. [20] is a reaction between water and Zr-O-Zr bonds at the crack tip during the transformation in Y-and Ce-ZrO_2. The results showed similar values for the reactions. Therefore, it was assumed that water react primary with Zr-O-Zr bonds on the surface and not the stabilizing oxide.
Yoshimura et al. [21] reported the role of penetration of OH molecule on the degradation in Y-TZP in several steps as follows:
Step 1: Chemical-adsorption of H_2O at the surface.
Step 2: The formation of Zr-OH and/or Y-OH bonds at the surface.
Step 3: The migration of OH^- ions at the surface and in the lattice so nucleating defects are prepared.
Step 4: The nucleation of monoclinic phases in the tetragonal grains.
Chevalier et al. [22] showed that LTD undergoes a nucleation and growth mechanism. The nucleation of transformation on one grain leads to a volume increase stressing up the neighbouring grains resulting in microcracking which offers a way for water to penetrate the specimens, see Fig. 1.5. The extension of transformation occurs preferentially in the neighbouring grains. Nucleation takes place on the most unstable grains that are subjected to the highest internal/applied tensile stresses. The unstable grains can be those with less Y_2O_3 or and with large size and/or subjected to higher internal stresses.

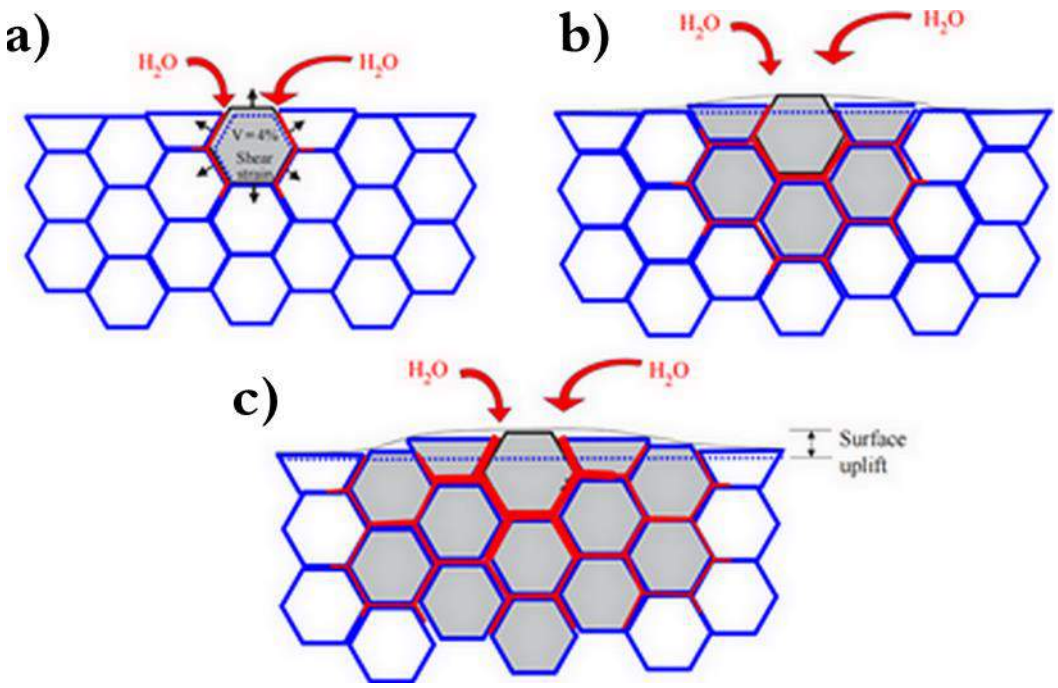

Fig. 1.5 Illustration showing the transformation neighbour to neighbour (a), nucleation on a particular grain at the surface (b) and (c) growth of the transformed zone [23].

The number of nuclei increases with the stresses because of the penetration of water. Simultaneously, a growth mechanism takes places because the transformation of one grain puts its neighbours under tensile stresses, favouring their transformation under the effect of water. The kinetics of aging was described using Mehl-Avrami-Johnson (MAJ) laws in which time and the amount of monoclinic phase is described as the following:

$$f = 1 - exp[-(b.t)^n] \tag{1.5}$$

where, f is the transformation fraction, t is the time, and b and n are constants. The exponent n is related to the nucleation and growth conditions. The parameter b is related to the activation energy Q and it depends on temperature and follows an Arrhenius law in temperatures between 37-140 °C:

$$b = b_0 \, exp\left[-\frac{Q}{RT}\right] \tag{1.6}$$

where b_0 is a constant, R the gas constant and T the absolute temperature.
An increase of monoclinic phase with increasing aging time has been reported by Chevalier at al. [22] at different temperatures (70-130 °C), see Fig.1.6. The results show an incubation-nucleation-growth mechanism of transformation because of the sigmoidal variation of the monoclinic phase with time for all temperatures.

A linear relationship for each temperature with a constant value of n equal to 3.6 was observed which fits very well with the experimental data. This value between 3 and 4 corresponds to a nucleation and three dimensional growth process according to the MAJ model. Therefore, the MAJ model gives a good prediction of monoclinic phase at the surface of aged 3Y-TZP for a given time and especially low temperature.

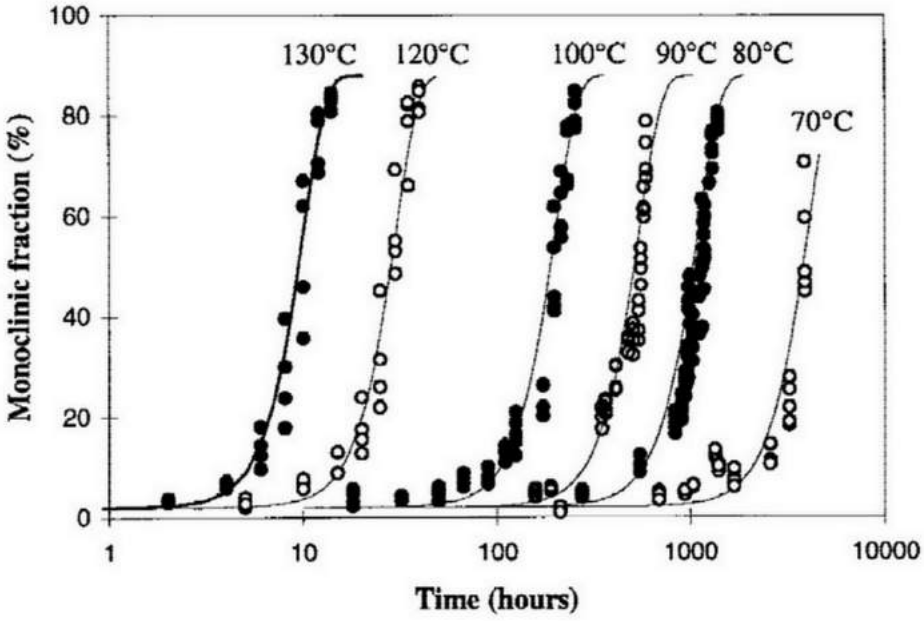

Fig. 1.6 Monoclinic phase versus time from a temperature range 70-130 °C [22].

There are many factors influencing the LTD such as the density, grain size, the homogeneity of the phase distribution and the residual stresses on the surface. For instance, the low density together with the presence of open porosity allow water molecules to penetrate into the bulk resulting in microcracking and pores and then leading to a drop in the mechanical properties.

Grain size has also a strong influence on LTD of zirconia. It was widely reported in the literature [24–26] that a decrease in the grain size (200 nm) limits aging. But, a reduction of grain size induces a decrease of toughness because of the transformation toughening. Indeed, a decrease of grain size influences the surface term in equation (1.1) where this latter leads to a dependence of the activation barrier for *t-m* transformation on the particle size. Hence, the activation barrier for the formation of critical nucleus is increased by a decrease in particle size.

A bimodal microstructure of 3Y-TZP appears when it is sintered at high temperature and consists of cubic and tetragonal phases. The cubic grains are larger than the tetragonal ones which pump the Y_2O_3 out. The tetragonal grains are depleted and less stable. Thus, they act as nucleation sites [27–29].

The stress distribution plays a critical role in transformation. The microscopic tensile stresses in a grain trigger the *t-m* transformation. Schmauder and Shubert [30] reported

that unconstrained grains were stable under humid conditions, whereas constrained grains transformed. The principal stresses from the thermal expansion anisotropy enhance the transformability of tetragonal grains to the monoclinic grains by increasing the *t* driving force and lowering the nucleation barrier.
Increasing the amount of Y_2O_3 stabilizer increases the resistance to LTD. It was reported that 4 mol % yttria stabilized zirconia shows better resistance to LTD compared to the 3 mol % yttria stabilized zirconia [31].

1.1.6 Applications of zirconia ceramics

Zirconia ceramics are used in wide range of applications: a dental bridge, oxygen sensors, grinding media, fuel cells, cutting blades, knifes and bearings for example. However, its main use is in the medical sector because of its outstanding mechanical properties, especially its unique balance of toughness and strength compared to other ceramic oxides, as well as biocompatibility. More than 60000 zirconia femoral heads have been implanted in the United States and Europe. Later on, 400 femoral heads have failed due to aging which resulted in a catastrophic impact on the use of zirconia in the medical sector. In the same time, results showed excellent behaviour of some heads after several years in vivo [23]. Therefore, the correlation between aging and clinical failures is still a matter of debate. The orthopaedic market sale decreased more than 90 % between 2001 and 2002 [3].
On the other hand, the aesthetic appearance in combination with excellent mechanical properties makes zirconia an excellent choice to be used in restorative dentistry. Zirconia has been used as implants and implant abutments, orthodontic brackets, cores for crowns, included endodontic posts and fixed partial denture prosthesis (FPDP) framework. As the grain size strongly affects the mechanical properties and aging, the grain size of 3Y-TZP used in dental applications consists of small equiaxed grains in the range of 0.2–0.5 μm depending on the sintering temperature [32]. The flexural strength of zirconia used in restorative dentistry is ≈ 1000 MPa and the indentation fracture toughness of ≈ 7 MPa√m [33].

1.2 Carbon Nanotubes

Nowadays, carbon nanotubes (CNTs) are considered as one of the most important nanomaterials making the next industrial revolution. They are used in many applications such as: electronics, semi-conductors, aerospace, etc. Their extraordinary properties are the key behind the high demand.

1.2.1 Structure of Carbon Nanotubes

In 1985, a new form of carbon C_{60} called the fullerenes [34] was discovered by Harold Kroto, Richard Smaley and Robert Curl (Nobel prize in chemistry in 1996). The main objective of their work was to determine the nature of carbon "clusters" present in interstellar space. Later on, intensive investigations were conducted from all over the world on the new carbon allotropes.

In 1991, Iijima [35] observed for the first time multi wall CNTs (MWCNTs) and later in 1993, he discovered single wall CNTs (SWCNTs) [36]. Fig.1.7 shows different types of CNTs. CNT has a cylindrical form; it can be seen as a rolled plane of graphene. Its diameter is in the nanometric scale and its length can be in several centimetres which lead to a high aspect ratio (length/diameter) of more than 10^7. CNTs have unique properties. They have a high Young's modulus (≈1500 GPa), high tensile strength (≈100 GPa), significantly higher than steel and carbon fibres, high thermal conductivity which is higher than diamond and an electrical conductivity similar to silver and platinum. The density of CNTs is much lower than aluminium [6][37].

Depending on the number of graphene cylinders (x), CNTs are referred to as SWCNTs (x=1), DWNT (x=2) and multi wall CNTs (MWCNT) with x> 2.

For MWCNTs, the interspace between two successive CNTs is in the range from 0.344-0.36 nm and the carbon nanotube bond length is 0.144 nm [37]. SWCNTs can be visualized as a single sheet of graphene wrapped up to form a tube and for most observed SWCNTs, the diameter of the cylindrical graphene sheet is <2 nm.

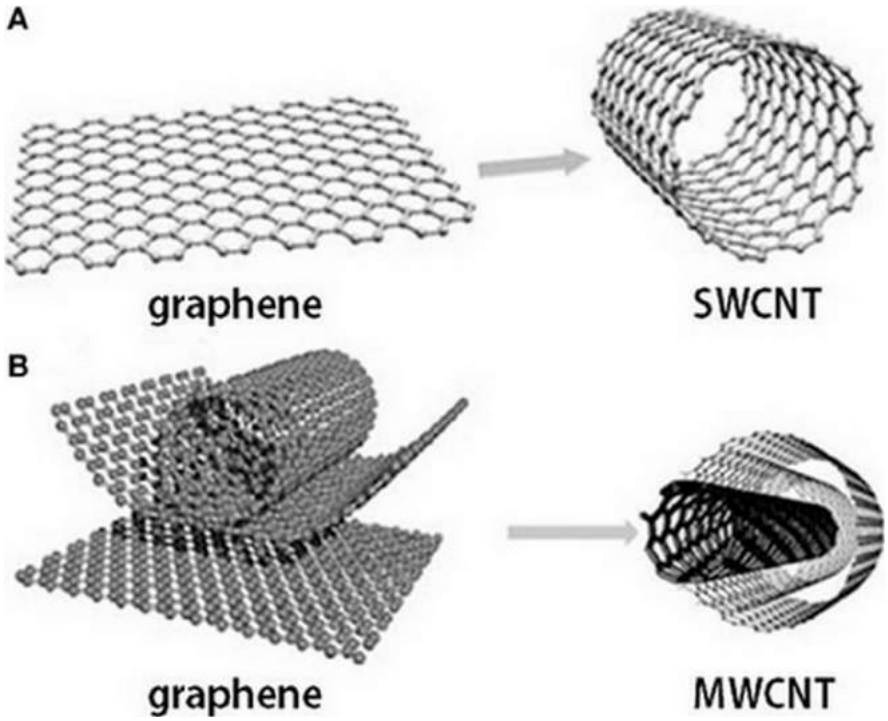

Fig.1.7 Different types of CNTs based on their number of graphene cylinders: (a)capped single wall CNT (SWNT); and (b) open multi wall CNT (MWCNT) [37].

Looking into the structure of a carbon nanotube, an orientation of the six-membered carbon ring (hereafter called hexagon) in the honeycomb lattice relative to the axis of the nanotube is observed. Three examples of SWNTs are shown in Fig.1.7. The direction of the six-membered ring in the honeycomb lattice is almost random and any distortion can be seen except the distortion in the ends of the cylinder due to the curvature of the carbon nanotube. Therefore, many structures for carbon nanotubes are made possible based on the symmetry of the carbon nanotube bonds [38].

The classification of carbon nanotube is either achiral (symmorphic) or chiral (non-symmorphic). In an achiral carbon nanotube the cylindrical structure follows mirror symmetry in both axes, longitudinal and transverse. Depending on the cross-sectional ring the achiral nanotubes can be armchair or zigzag nanotubes as shown in Fig.1.8. In chiral nanotubes, the mirror symmetry is not obeyed. The axial chirality is commonly discussed in relation to optical activity [38]. There is another structure that comprises several truncated conical graphene layers called cup-stacked [38]. The numerous ways to roll graphene into tubes are mathematically defined by the vector of helicity $\bar{C}$ and the angle of helicity θ as shown in Fig.1.9 and can be described in equations (1.7) and (1.8):

$$\bar{C} = n\overrightarrow{a_1} + m\overrightarrow{a2} \tag{1.7}$$

$$\theta = \tan^{-1}\left(\frac{m\sqrt{3}}{m+2n}\right) \tag{1.8}$$

where n and m are integers and they can be grouped together to make lattice translational indices (n, m). The verctors $\overrightarrow{a_1}$ and $\overrightarrow{a_2}$ are the vectors of the hexagonal lattice that corresponds to a section of the nanotube perpendicular to the nanotube axis (see fig.1.9). The angle of helicity θ is the tilt angle of the hexagons with respect to the rolling axis and determines the spiral symmetry. Due to the six fold symmetry of the honeycomb lattice, the value of angle of the helicity θ falls in the range $0°$-$30°$. When $n = m$, the nanotube is armchair type ($(\theta = 0°)$, when $m = 0$, then it is of the zigzag type and when $n > m > 0$ it is chiral, see Figs. 1.8 and 1.9.
The chirality of CNTs affects the optical, mechanical and the electronic properties. CNTs are metallic when $|n - m| = 3q$ and they are semiconductors when $|n - m| = 3q \pm 1$ where q is an integer [38].

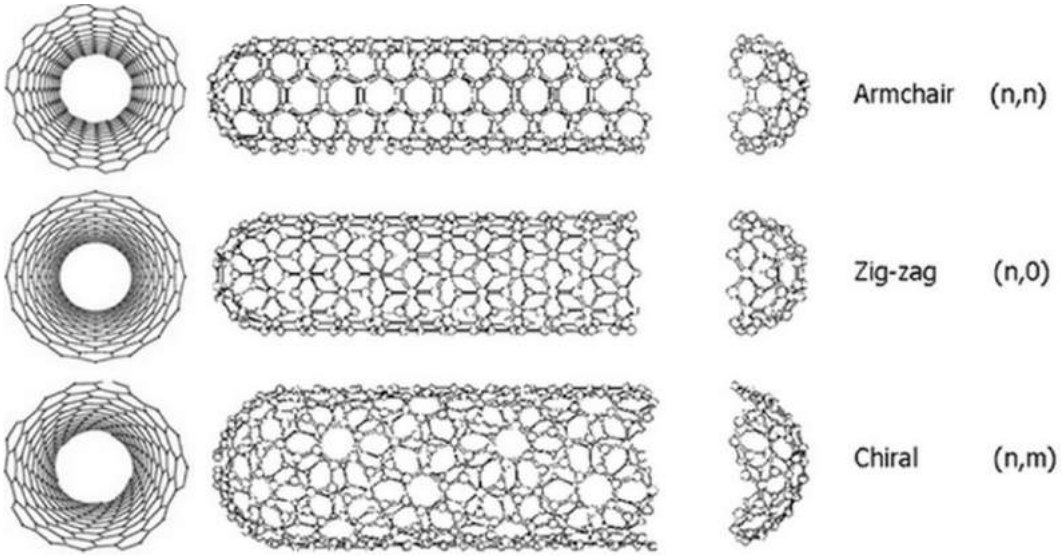

Fig. 1.8 The terminations of each of the three types of nanotubes. The terminations are often called caps or end caps and consist of a "hemisphere" of a fullerene. The figure shows as well the different types of CNT based on the chirality [38].

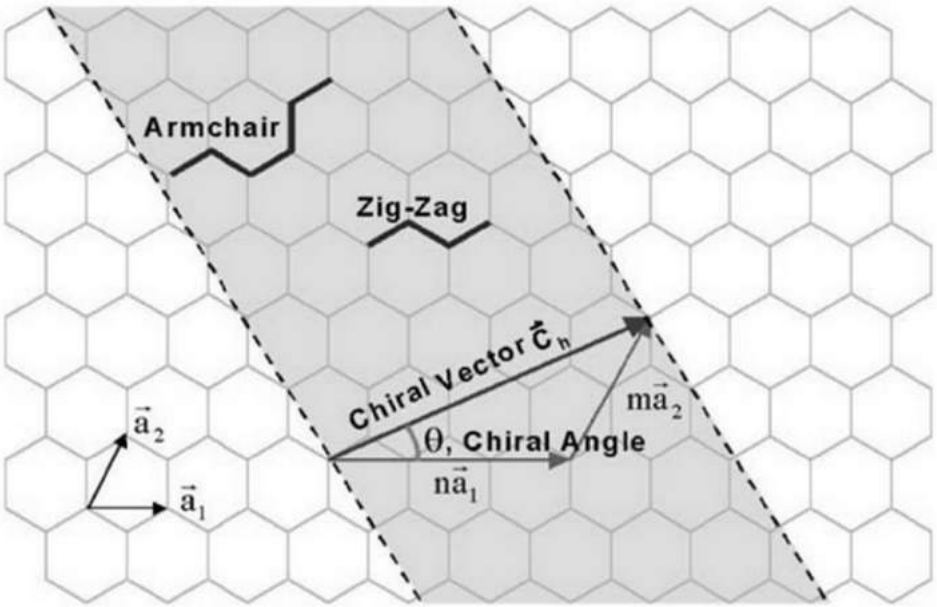

Fig.1.9 Schematic showing how a hexagonal sheet of graphite is "rolled" to form a carbon nanotube [39].

1.2.2 Synthesis of CNTs

There are several methods to produce CNTs in which the quality depends on the method of synthesis.

CNTs were first synthesized using high temperatures, such as in arc discharge or laser ablation. However, nowadays, other methods are used for a better control of the synthesis of CNTs, for example, Chemical Vapour Deposition (CVD). The orientation, the purity and the density of CNTs can be controlled using CVD. Moreover, there are other methods based on the use of gas-phase that are found to be more convenient for composite materials where the production of large quantities is required.

On the other hand, all methods used for the synthesis of CNTs induce impurities such as nano-crystalline graphite, amorphous carbon, fullerenes and different catalysts: Fe, Co, Mo and Ni. The impurities decrease the mechanical properties of CNTs. Therefore, acid treatment has been used as an efficient and simple purification method for CNTs.

Arc discharge

The arc discharge method is a simple method for the synthesis of CNTs at high temperatures (>1700 °C). For MWCNTs, arc discharge is based on using DC arc discharge between two graphite electrodes, usually water-cooled in a chamber filled with helium (He) at sub-atmospheric pressure. He atmosphere was used by Iijima et al. [35] for the synthesis of fullerenes in order to obtain first scale synthesis of CNTs. Zhao et al. [40,41] used He and methane gases and they resulted in different CNTs

morphology. A study by Wang et al. [42] has confirmed that the use of different atmospheres strongly influences the morphology of CNTs. On the other hand, synthesis of CNTs in liquid solutions has also been studied. Thus, Jung et al showed that the use of arc discharge in liquid nitrogen results in high yield MWCNTs.
In the case of SWCNTs, the synthesis by arc discharge implies the use of a composite anode in hydrogen or argon atmosphere. The anode is made of graphite and a metal such Ni, Fe or Co. The anode can also be a mixture of a metal and another element like: Co-Ni, Fe-Ni, Fe-No. Iijima and Ichihashi [36] reported the first synthesis of SWCNTs with a diameter of 1 nm. Then, Berthune et al. [43] reported the synthesis of SWCNTs by Co catalysis with a diameter of 1.2 nm. Saito et al. [44] reported growing of SWNTs radially from Ni fine particles. In 1996, they investigated the use of platinum group metals (Rh, Pd, Os, Ir, Pt) in the synthesis of SWCNTs by arc discharge [45]. Later on, a new approach was reported based on using a hydrogen DC arc discharge called ferrum-hydrogen which results in a high crystallinity of SWCNTs [46,47]. Moreover, a cheap method was reported for the synthesis of high purity SWCNTs with a diameter of 1.2 nm. The method was based on the synthesis of SWCNTs in argon DC arc discharge from charcoal as carbon source and FeS as catalyst [48].

Laser ablation

Pulsed laser deposition (PLD) used for the synthesis of CNTs is similar to the arc discharge, where this time the energy is provided by a laser hitting a graphite pellet containing nickel or cobalt as catalyst material. Laser ablation is considered as a superior method for the production of SWCNTs with high quality and purity [49]. The lasers used for ablation have been Nd:YAG and CO_2. Some studies reported that the use of a continuous wave of CO_2 laser ablation without any additional heating to the target and with increasing the laser power will increase the average diameter of SWCNTs. A study by Kusaba and Tsunawaski [50] showed that using a laser ablation at 1623 K with oscillation wavelength of 308 nm irradiating a graphite containing Co and Ni at various temperatures resulted in the highest yield of SWCNTs with the diameter between 1.2 and 1.7 nm.

Chemical vapour deposition

The catalytic chemical vapour deposition (CCVD) is considered as an economic and practical method for the production of CNTs with high purity and more controlled production compared to laser ablation. Thus, CVD is now a standard method for the production of CNTs. The models presented by Fotopoulos and Xanthakis [51] suggested that SWNTs are produced by based growth where the cap is formed first, and then the CNTs are fabricated by addition of carbon atoms at the base.

The most used catalysts in CVD are Fe, Co, or Ni [52]. The catalysis contributes to the decomposition of carbon source by plasma irradiation or heat and to the nucleation of CNTs. The carbon source used in CVD is hydrocarbons while the substrates commonly used are Ni, Si, SiO_2, Cu, Cu/Ti/Si, stainless steel or glass [53,54].
A study by Flahaut et al. [55] reported the influence of catalyst conditions on the synthesis of CNTs by CCVD. They observed that the combustion conditions in the case of using citric acid as a catalyst can induce either an increase in the CNTs walls or limit the formation of carbon nanofiber. Lyu et al. [56] used benzene as an ideal carbon source and Fe-Mo/Al_2O_3 as a catalyst at 900 °C and they succeeded to produce high-quality and pure DWCNTs.
Cui et al. [57]used acetonitrile as the carbon source and the ferrocene as the catalyst and they could produce thin walled, open-ended, and well-aligned N-doped CNTs on the quartz slides that can be used in many applications.

1.3 Processing of zirconia–CNT composites

1.3.1 Dispersion of CNTs

The synthesis methods reported in section 1.2.2 result in production of CNTs with different physical entanglement of the nanotubes where individual CNTs are entwined, interwoven and agglomerated. Therefore, the dispersion of CNTs is considered as a crucial step and a challenge in the processing of ceramic-CNT composites. A chemical entanglement can occur when a surface-surface attraction takes place. Moreover, the high aspect ratio, the high flexibility of CNTs increases rapidly the chance of entanglements. Besides that, attractive Van der Waal's forces between carbon surfaces increase the difficulty of CNTs to be dispersed. The molecular forces between carbon nanotubes are influenced by both chirality and surface curvature [58].
The objective of dispersion is to produce independent separated tubes that can be oriented either in one dimension (fiber), two dimensional (flat sheet) or three dimensions (bulk solid). The dispersion can be physical (mechanical) or chemical. Mechanical dispersion consists of separating the tubes by using ultrasonication for example. Chemical dispersion is based on functionalization using solvents or surfactants to change the surface energy of the nanotubes. The functionalization of the tubes may improve their adhesion characteristics to the matrix and helps to reduce agglomerations. On the other hand, the use of aggressive chemical or mechanical dispersion will result in changes in CNTs properties [58].

The ultrasonication

Ultrasonication method is usually used to improve the dispersion of CNTs by shortening the tubes. However, there is a risk that the tube-wall will be damaged or broken. Therefore, an advance ultrasonication method based on the use of diamond crystals is developed where the SWCNTs bundles are destroyed but not the tubes. For MWCNTs, it was reported that the ultrasonication seems to destroy the external layers, so MWCNTs will not only get shorter but also thinner with time [59]. Moreover, ultrasonication can be used to remove impurities. A study showed that CNTs has been purified from ≈70% to ≈90% by ultrasonication-assisted filtration [60].

1.3.2 Sintering

Sintering is a thermal treatment of powder compacts at temperature below the melting point resulting in dense polycrystalline solid. Thermodynamically, sintering is an irreversible process in which free energy decreases is brought by a decrease in surface energy. The main methods of sintering are described below.

Hot Isostatic Pressing (HIP)

Hot Isostatic Pressing is a technique invented in United States in order to diffuse bonding nuclear fuel element assemblies [61]. HIP was first used to bond materials using high temperature and isostatic pressure. Therefore, it was called Gas Pressure Bonding [62]. High performance and high temperature ceramics such as silicon nitride and silicon carbide were the first to be produced commercially. Moreover, HIP was used to produce alumina cutting tools with excellent cutting properties at a reasonable cost. Later on, HIP was spread to oxide ceramics such as Mn-Zn ferrite, PZT and PSZ being one of the most promising technologies produce parts with good mechanical strength and reliability [63] .

The advantages using HIP lies in the high densification, elimination of porosity, improvement of fatigue properties, improvement of creep properties, improvement of ductility and strength and recovery of defective parts. Besides that, it has been found that HIP can achieve a desired shape with a high degree of control and accuracy [61,64,65].

HIP equipment consists of an electric furnace contained in a pressure vessel. The high pressure transmitting gas which fills the pressure vessel is argon gas because the viscosity of the gas is very low and its density is very high. As a consequence, the heat generated by the heating is transferred by the natural convection of the gas. The furnace, the heating device and the heat insulation are made of heat resistant alloys or refractory metals [61].

Spark Plasma Sintering (SPS)

Sintering under an electric current was first patented in 1906. In 1960, an invention of Spark sintering based on pulsed current was reported. However, the high equipment cost and the low sintering efficiency limited its wider use. The concept was further developed and in 1990s, Japanese companies, in particular Sumitomo Coal Mining Co. Ltd started the industrial production of Spark Plasma Sintering machines based on the use of pulsed direct current to heat the specimen. Later on, FCT System GmbH in Germany and Thermal Technology LLC, Inc. in the USA started producing similar equipment based on pulsed DC current. Today, the number of SPS machines installed in the world reaches 1750 with 2/3 in the industry. Besides that, more than 3000 publications have been reported using this technique and its applications according to the ISI Web of Science [66].

The configuration of SPS consists of a uniaxial pressure system, together with a high power electrical circuit placed in a controlled chamber. There is also a pulsed direct current (DC) generator, water cooled reaction chamber, a pressure-, a position- and temperature-regulating systems. The powder is located into the die, and a mechanical pressure is applied during the sintering process, see Fig.1.10.

A low voltage typically below 10 V is applied leading to an efficient Joule heating that goes through the sample. Even in the case of non-conductive ceramic powder the heat is efficiently transferred to the sample. Rapid heating rates could reach 1000 °C/min reducing the duration of the process and the energy costs [66]. Moreover, cooling rates of 150 °C/ min are also possible. The mechanical pressure applied to enhance the densification could be as high as 50 to 250 kN. The densification takes place under vacuum or protective gas. Finally the maximum temperature using standard graphite tools could attain 2400 °C where either thermocouples or axial/radial pyrometers are used to control the temperature.

It was reported that when using non-conductive powder together with the use of an electrically conductive die, the current will be forced to pass through the powder generating the highest possible current density, see Fig.1.11.

The stress applied in SPS induces changes in the morphology of contact between the particles and enhances the densification mechanisms. The grain growth during sintering is usually delayed and reduced. However, the grain size can be several times larger than the initial particle size as was reported for several oxides densified by SPS and HP [67]. It was reported that a finer starting particle size, in the opposite of coarser one, may induce a larger grain size at full density [68].

By increasing the pressure during SPS, the agglomeration breaks. At low temperature, the particle rearrangement increases reducing the pore size which enhances densification and limits the grain growth. At high temperature, other mechanisms take place such as plastic deformation or power law creep. Thus, low temperatures are needed for full densification [66].

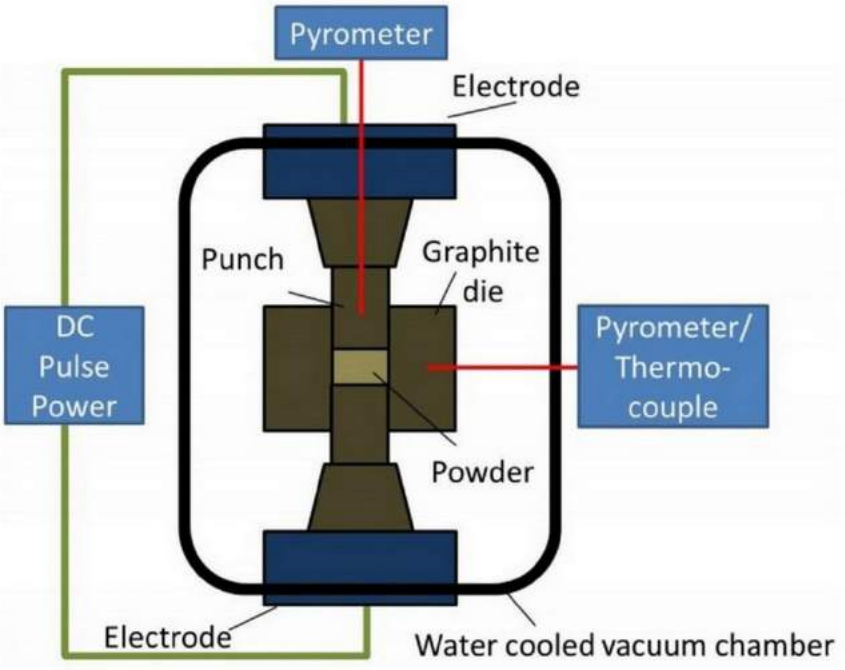

Fig.1.10 Schematic of SPS showing the different parameters involved during sintering [66].

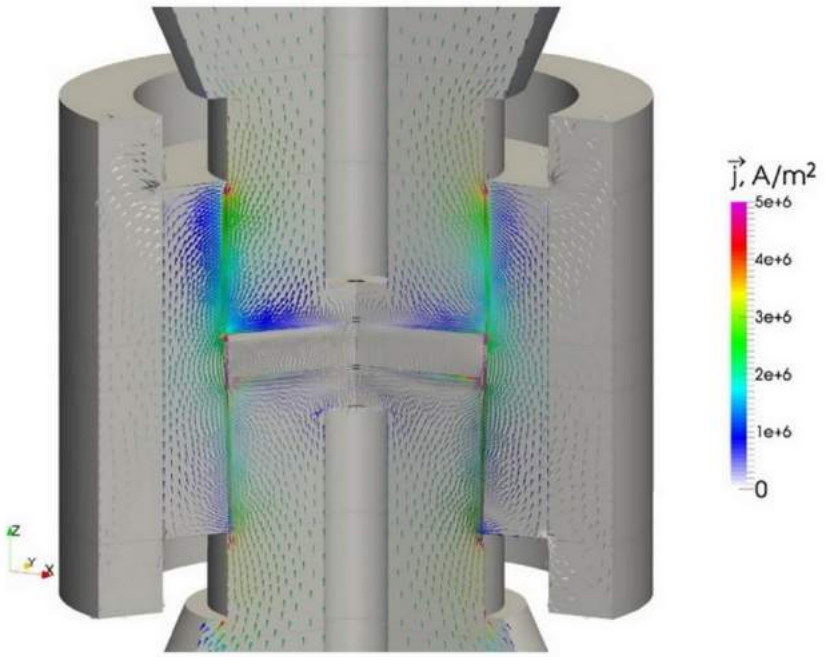

Fig.1.11 Schematic of current flow in case of non-conductive powder and a conductive die [66].

CHAPTER 2

Properties

2.1 Mechanical properties

2.1.1 Reliability of indentation fracture toughness

Measuring fracture toughness using indentation method has always been a matter of dispute. The origin of indentation fracture toughness was first initiated in 1970 by Evans and Charles [69] in a short communication. Then, the indentation technique achieved a high popularity because of its expediency. Moreover, it needs a short time for preparation and it is not costly. Therefore, the use of indentation method is practically ideal even if it is reported that it is not an accurate method for the determination of fracture toughness.

The indentation technique described by Evans and Charles [69] suggests using the cracks which emanates from the corners under a high testing load. They presented a generalized equation and a normalized calibration curve that appeared to apply to many different materials with Palmqvist cracks or with median cracks. Later on, several authors have used similar curve fitting methods. However, many researchers have been confused with their results using the indentation method which have led to the issue of more than 30 equations presented in literature [70].

Indentation fracture toughness consists of the preparation of a high quality smoothly polished surface. Then, the polished surface is indented by a Vickers pyramidal hardness indenter. The sample is indented at high testing load until a deformed region is created beneath and in the vicinity of the indent. As a consequence cracks are generated from the four corners of the impression, see Fig.2.1. The indentation is not always perfect, for example it can lead to spalling chipping at high test loads. The parameters involved in calculating the indentation fracture toughness are: the lengths of the cracks, indentation load, impression size, the hardness and elastic modulus and a calibration constant. One should take care while measuring the lengths of the cracks

Depending on the load and the multiple cracking, the material surrounding the

impression could be left with a complex residual stress state. Therefore, there are many questions raised concerning the sequence of crack growth from the Vickers indentation corners. It could for example be that the cracks first form Palmqvist cracks that can extend to median cracks or it could be that median cracks form directly from the deformation beneath the indenter. Furthermore, the cracks could be formed either during indenter loading or unloading. Besides that, the environment such as the water vapour may affect the results [70].

As mentioned before, there are numerous equations reported to calculate the indentation fracture toughness. Most of the equations are only a manipulation of previous equations with new calibration constants. Moreover, most of the equations proposed are highly questionable because of their lack of an accurate stress intensity factor solution. Furthermore, the complex network and the residual stress damage zone around indentations are not helpful to give a direct analysis as in traditional fracture mechanics tests.

However, the most frequently used equations after Evans and Charles [69] are the ones of Marshall and Evans [71] who simplified the formula of indentation. Afterwards, there are Anstis et al. [72] who proposed additional modifications to the proposed equations. Then, two more papers were published by Niihara [73] describing the Palmqvist cracks. Finally, an adaptation of the equation of Anstis et al. [72] was reported by Miyoshi et al. [74] for median cracks.

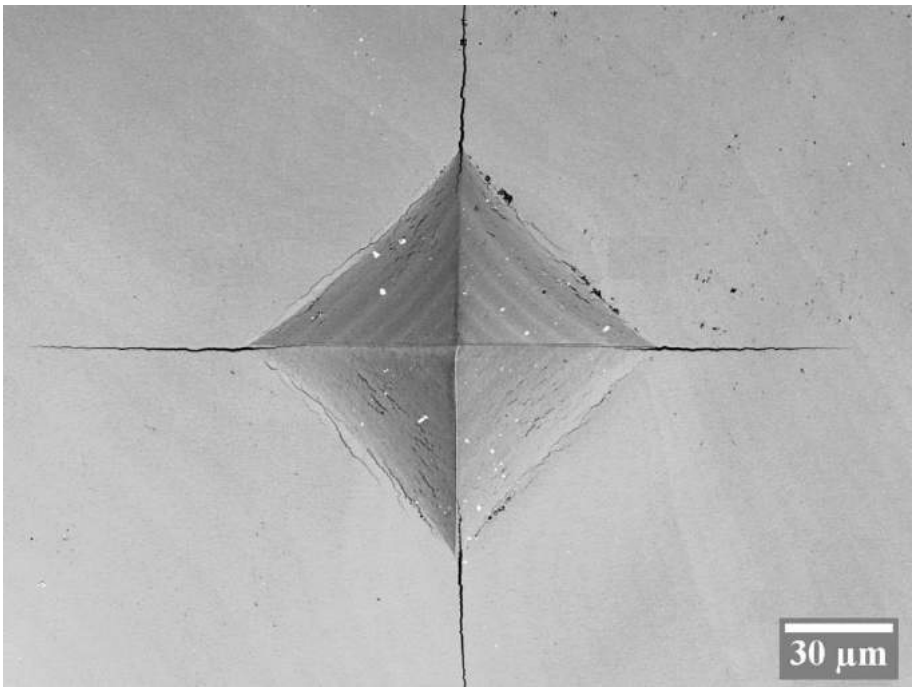

Fig.2.1 Vickers indentation with cracks formed under 10 Kg load in SPSed zirconia.

2.1.2 Comparison between indentation method and standardized fracture toughness tests

The geometry in a standard fracture toughness test is simple and the crack has well-defined shape for which loading conditions in addition to the state of stress are known. For the indentation method, any geometry can be convenient as long as it can be mounted and polished. Moreover, there is no pre-crack in the specimen subjected to an indentation test. There are cracks that are generated when the indenter is forced into the polished specimen surface. However, in standard tests, there is a single well-defined pre-existing crack for which there is a formal stress intensity solution. The loading in standard test is done using a universal mechanical testing machine and a prismatic specimen where a sharp notch is machined through the specimen. For indentation method, under loading, plastic deformation occurs below and around the indentation which results in multiple cracks that propagate beneath the indenter in addition to high complex residual stresses. In fact, the method is based on a model of the residual elasto-plastic stress field which depends on the material and on the assumption that this field can be represented by an opening force on the centre of the indentation. For quantitative estimations the equation of the stress intensity factor is calibrated by a constant from the fracture toughness determined using standard methods.
Li et al. [75], Ponton and Rawlings [76] and Ghosh et al. [77] discussed the credibility of the different equations used for the indentation method and they revealed its weakness by summarizing indentation results using different equations for the same materials. The most critical conclusions of the four publications are summarized as follows:

1) The different proposed equations for the calculation of fracture toughness for the same or closely the same crack length in ceramic materials result in wide range of different K_{IC} results.
2) The equations proposed are not able to generate accurate results for different materials.
3) The different equations result in increase or decrease of fracture toughness depending on the crack length for the same material. Moreover, the "R-curve" behaves differently for the same material when the different equations for the calculation of indentation fracture toughness are applied.

The above conclusions illustrate clearly the inadequacy of using indentation method. The first conclusion shows that indentation method does not result in unique value of K_{IC}. The wide range of K_{IC} results obtained by using indentation method indicates its unreliability in measuring the true K_{IC} of brittle materials. In addition, brittle materials deform and fracture differently underneath an indentation. Ceramics with covalent bonding such as silicon carbide deform differently than the ceramics with ionic bonding such as magnesium oxide or glasses. Furthermore, fine grain and coarse grain ceramics have different fracture mode as well. Moreover, the indentation cracks are three

dimensional networks. Therefore, the cracks cannot be idealized as Palmqvist, semi-circular or median as it is assumed in the equations proposed.
The variation of indentation fracture toughness with the crack length seems to be in a contradiction with the R-curve of brittle ceramics. The R-curve is either flat as for fine-grain ceramics or increases with crack length as for coarse grained polycrystalline ceramics. R-curve should not be decreasing with increasing the crack length, as was reported in conclusion 3 which makes the indentation method results confusing.
As summary, it is concluded that the different equations proposed for the calculation of indentation fracture toughness in the literature are not reliable.
Therefore, indentation fracture is not a suitable method for the calculation of fracture toughness. For this reason, we have in the current work developed, a new testing method from the measurement of the "true" fracture toughness of small cracks [78].
The new method is based on inducing a very sharp shallow surface notch using Pulsed Laser Pulsed Ablation (UPLA) on the surface of prismatic bars which was parallel to the original discs and determining the "true" K_{IC} from the strength in four point bending [78]. More details on the experimental procedure will be discussed in Chapter 3. See Fig.2.2 shows an example of a notch induced by UPLA.

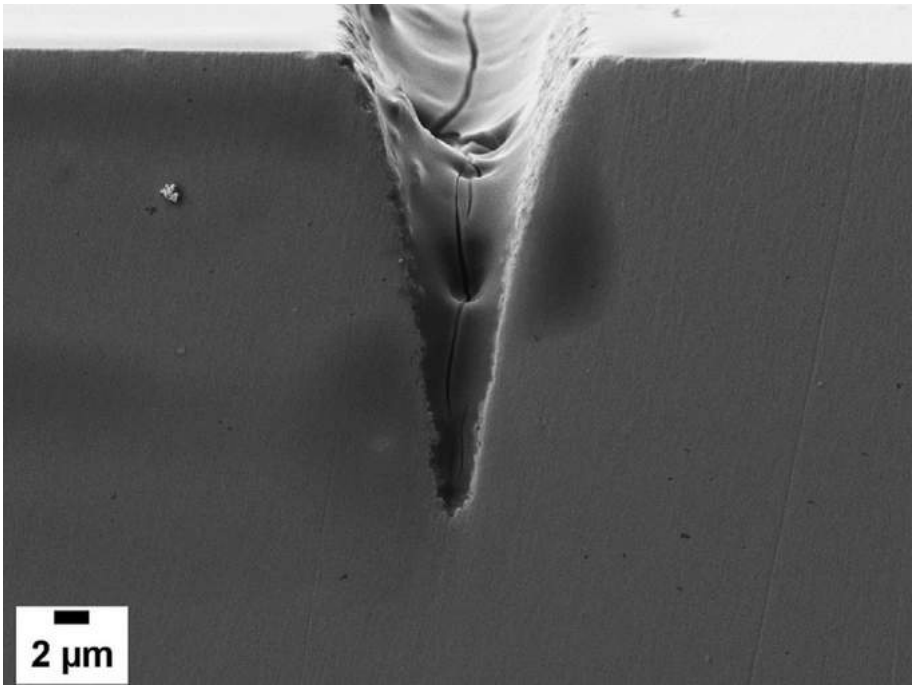

Fig.2.2 Side view of the notch induced by UPLA on SPSed zirconia.

2.1.3 Effect of CNTs on the mechanical properties

It was reported that a single CNT failed after 280 % stretching at high temperature [79]. A study by Treacy et al. [80] reported individual CNTs with Young's modulus of more than 3 TPa. Lourie et al. [81] estimated that the stress required for producing buckling or collapse of CNTs is around 100-150 GPa. Therefore, it is evident that CNTs are the strongest and the stiffest fibres ever found. However, the efficiency of the addition of CNTs in improving the mechanical properties of ceramic matrix composites is still a matter of debate.

Mukhopadhyay et al. [85] reported that the crack bridging provides a 150 % improvement of the fracture toughness compared to a monolithic material and that no fibre pull could be detected. A study carried out by Estili et al. [84] showed that the different toughening mechanisms such as crack deflection, fibre pull-out or crack bridging of CNTs induce an increase of 67 % of the fracture toughness with the addition of 3.5 vol % MWCNTs to alumina matrix. However, the hardness and elastic modulus were decreased with the addition of CNTs in the matrix. Moreover, An et al. [86] showed that the strong bonding between the matrix and MWNTs result in the improvement of elastic modulus from 74 GPa to 118 GPa by adding 6.4 vol % MWNT to silicon carbonitride (SiCN) matrix.

On the other hand, as it was described in the previous section, the use of the indentation method results in a big dispersion of different K_{IC} values in literature.

A study by Zhan et al. [82] of the addition of SWCNTs in alumina nanocomposites showed a high increase of indentation fracture toughness (9.7 $MPam^{1/2}$) and a decrease in hardness of about 20 %. However, Wang et al. [83] had ambiguous results by the use of indentation method in the determination of fracture toughness. Therefore, they used single edge V-notch beam (SEVNB) on the same composites and they showed an improvement of only 3 % in fracture toughness. Nevertheless, they used a razor notch radius which is not sharp enough, see Fig.2.3. The study by Wang et al. [83] also reported that alumina-graphite composites prepared by SPS do not have a high fracture toughness, but they have a good contact-damage resistance. SWCNTs are highly shear-deformable which induce an intensive confined-shear field and causes a redistribution of the stress under the indenter which prevents the formation of cracks. Melk et. al [78] studied the addition of MWCNTs to zirconia matrix and they showed that the "true" fracture toughness of the composites is hardly increasing while the indentation fracture toughness is increasing which indicate that the incorporation of CNTs to zirconia matrix increases the resistance to cracking under contact loading.

In 2007, Quinn and Bradt [84] suggested strictly to not use the indentation method for the determination of fracture toughness.

Sun et al. [97] and Ukai et al. [98] showed that the addition of 1 wt % CNTs to 3Y-TZP/CNT nanocomposites induces no improvements of the indentation fracture toughness, fracture strength or hardness compared to 3Y-TZP matrix. They reported

that the low mechanical properties are due to the weak interfacial bonding between the matrix and the CNTs.

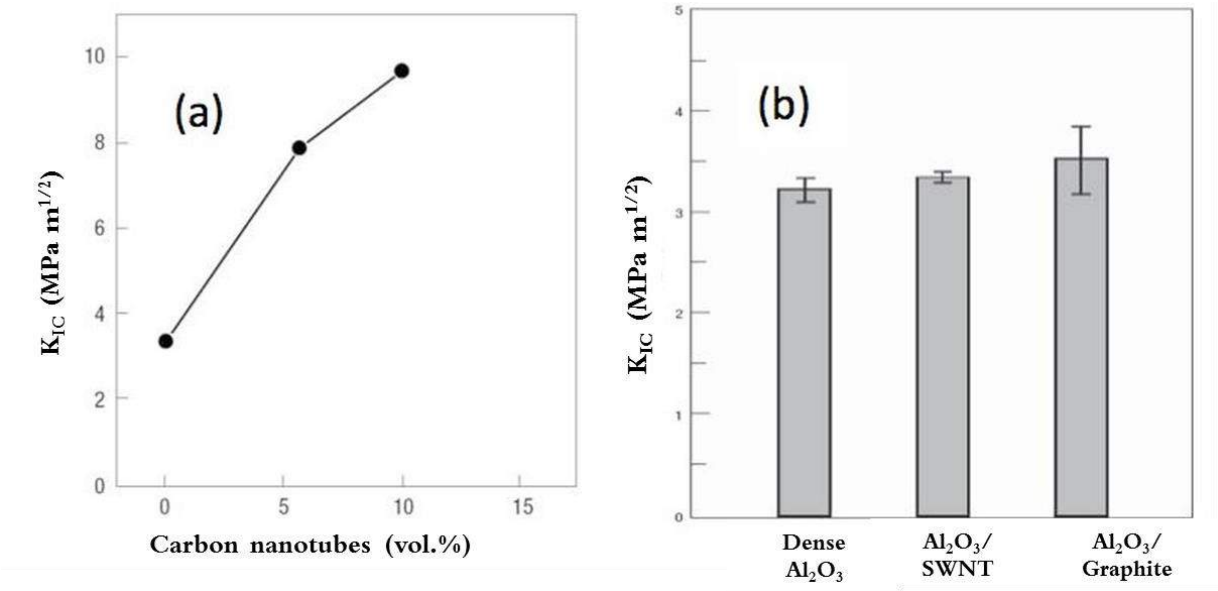

Fig.2.3 Fracture toughness of the SWCNT-alumina composites measured by (a) Indentation method measured by Zhan et al. [82] *and (b) SEVNB method measured by Wang et al.* [83].

Garmendia et al. [100] reported small improvements in indentation fracture toughness using slip casting for a better dispersion of carbon nanotubes in zirconia matrix. However, they found low Vickers hardness. Duszova et al. [6], [99] showed poor mechanical properties in hot pressed zirconia carbon-nanofiber composites. They reported that the composites have low density compared to monolithic zirconia.
Dusza et al. [101] used hot pressing and SPS for the sintering route of 3Y-TZP/CNF. The use of SPS showed higher indentation fracture toughness and hardness than the samples sintered by hot pressing. They concluded that using SPS for a short sintering time of only 5 min can prevent the nanotubes from oxidation and damage.
On the other hand, the addition of CNTs to alumina matrix has shown good results. It was reported by Fan et al. [88] that the addition of 1 % SWCNTs into alumina increases the indentation fracture toughness by 103 %. Moreover, Fan et al. [89] showed an improvement of 80 % of the indentation fracture toughness by studying hot pressed alumina-MWCNTs nanocomposites. However, Mo et al. used SPS for the processing of alumina-CNT and reported 7 % improvement of the Vickers's hardness and 10 % increase of indentation fracture toughness [87].
Chang et al. [92] and Siegel et al. [92] reported an improvement of 24 % of the indentation fracture toughness compared with a value of 4.2 MPa·$m^{1/2}$ of the monolithic alumina. However, Wei et al. [94] showed that by adding as little as 3 vol % CNTs to alumina matrix the indentation fracture toughness increases by 79 % and the bending strength increases by 13 %.

2.2 Tribological properties

The effect of CNTs on the tribological behaviour of ceramic-CNTs composites has mainly been studied in alumina-CNT composites. The first study was carried out by An et al. [85] on the wear mechanism of alumina-CNT composites. They reported a decrease in the wear loss of 56 % and an improvement of 30 % in microhardness. A study by Axia et al. [86] showed how well-aligned CNTs can determine the friction coefficient (COF) of the composites using pin-on-disc geometry. The highly ordered nanotube ceramic composites exhibited low COF and high wear resistance by tuning the CNT thickness and buckling properties. The authors reported 80 % reduction of the COF.

Studies of the tribological behaviour of CNT composites with zirconia as matrix material are fewer. In 2010, Hvizdos et al. [87] studied the wear behaviour of zirconia-carbon nanofiber (CNF) composites. They reported that the addition a little as 1.07 wt % CNF results in excellent frictional properties of the composites. The low friction coefficient achieved was related to the formation of a carbon-based transferred film on the surface which induces easy sliding and shear due to the lubricating effect of CNTs. Two years later, Hvizdos et al. [88] studied the effect of CNF/CNT on different matrix composites: ZrO_2, Si_3N_4, Al_2O_3. They showed the benefits of the presence of CNFs on the friction coefficient of the composites. They concluded that a small amount of CNFs can decrease the friction coefficient while the CNTs are less effective. Then, it is necessary to incorporate high amount of CNTs for better frictional results. The authors reported that the percolation of CNF occurred at ≈1 wt % CNF in ZrO_2 whereas, a percolation of 3 wt % and 5 wt % of CNT occurred for Si_3N_4 and Al_2O_3 respectively. Later, Kasperski et al. [89] used a pin on disc reciprocating flat geometry and an alumina ball as a counterpart for studying the tribological behaviour of 3Y-TZP/CNT composites in the range composition (0.55-5.16 wt % CNT). They reported that the composite with 5.16 wt % CNT had a coefficient of friction 3.8 lower than of monolithic zirconia and explained the obtained results by the exfoliation of MWCNTs due to the high shear stresses generated during sliding.

In the current thesis we have performed detailed studies of the frictional behaviour of SPSed 3Y-TZP/ CNT composites where a range of CNT content from 0 to 2 wt % were added to a zirconia matrix. It was found that the incorporation of 2 wt % CNT results in high wear resistance which to the best of our knowledge has never been reported before [90]. More details are reported in Chapter 4.

2.3 Electrical properties

The electrical conductivity of CNTs was found to be as high as $2 \cdot 10^7$ S/m [80]. The electrical properties of CNTs depends on the type, chirality and defects in the structure.

Therefore, adding a small amount of CNT to a ceramic matrix which is an insulator can make it a good conductor.

SWCNTs have better electrical conductivity properties than MWCNTs due to their perfect structure. The electron tunnelling between adjacent tubes in a percolated network of SWCNTs is believed to be the primary charge transport mechanism in CNT [91] . This mechanism has been associated with fluctuation-assisted tunnelling proposed by Sheng [92]. Sheng reported the observation of a new tunnelling conduction mechanism in carbon-PVC composite in which the modulation of tunnelling barriers by thermal fluctuations determines the dependency of conductivity on temperature and electric field [91].

Fonseca et al. [93] studied the electrical conductivity of 3YTZP/SWCNT composites in wide range of temperature. The authors attributed the high electrical conductivity of the CNT composites to the electron tunnelling between adjacent tubes in a percolated network.

The electrical percolation threshold in ceramic-CNT composites was reported to be very low due to the excellent electrical properties of CNTs. The addition of only 0.3 vol % CNTs to SiC matrix results in 75 % reduction of electrical resistivity [94]. Ahmed et al. [95] reported a high electrical conductivity with a percolation threshold close to 0.79 vol % attributed to the high aspect ratio of MWCNTs. A study by Inam et al. [96] reported higher electrical conductivity of alumina-CNT composites as compared to alumina black carbon. The high electrical conductivity was attributed to the large aspect ratio which results in entangled network of conductive paths. Furthermore, the use of SPS technique allowed lower sintering temperature and shorter sintering time which preserves CNTs from damage [66].

Hvizdos et al. [88] studied the effect of the addition of CNF to zirconia matrix. The authors reported an increase of electrical conductivity with the addition of 3 wt % CNF due to the formation of a continuous intergranular network of CNFs. Ukai et al. [97] showed that the addition of only 1 wt % CNTs results in improvement of electrical conductivity due to the formation of a 3D network structure of MWCNTs in the 3Y-TZP matrix.

In the current thesis, the electrical properties of zirconia-CNT composites produced using SPS have been studied. The incorporation of CNTs increases drastically the electrical conductivity of the composites when the percolation threshold is reached, which is only about s 1 wt % CNT [98]. More details are described in Chapter 4.

2.4 Electrical discharge machining (EDM)

As been described before in the introduction, 3Y-TZP has a wide range of applications due to their extraordinary properties: high strength, high toughness, good chemical resistance and biocompatibility compared to other oxide ceramics [99]. However, the main drawback of machining zirconia ceramics remain being the brittleness which limits their ability to be machined with conventional techniques such as cubic boron nitride (cBN) or diamond tools [100]. Nowadays, a successful and attractive machining technology based on the use of electrical discharge machining (EDM) allows machining complex shapes of electrical conductive materials with high precision up to the microscale level, being independent of the material hardness. In EDM, series of controlled electrical discharges are generated between a tool electrode and a workpiece immersed in dielectric fluid resulting in removing material from the workpiece mainly through melting, evaporation and spalling [101–103]. Nevertheless, EDM requires an electrically conductive workpiece, which limits its applications to nonconductive ceramics such as ZrO_2, Al_2O_3, Si_3N_4 and SiC [104–107].

It was reported that adding relatively large amounts of a conductive phase to 3Y-TZP such as WC, TiC, TiN, TiCN or TiB_2 [108–111] makes the composite electrically conductive and therefore, susceptible to machining by EDM. During EDM, the temperature raises and the melting temperature can be eventually reached which contributes to material removal. Some of the molten material disappears and some fraction of the melt solidifies on the EDM surface forming the recast layer. Melting has been observed mainly in metals as the main material removal mechanism [112]. However, Bonny et al. [113] reported full melting as material removal mechanism in the EDM of ZrO_2-WC composites. Melting was also observed in ZrO_2–TiN and Al_2O_3–SiC–TiC using wire EDM [108]. Lauwers et al. [114] reported the effect of microstructure on wire EDM in zirconia where 40 vol % WC was used as conductive phase. It was found that a finer microstructure results in a lower thermal conductivity and then a higher cutting speed for materials where the predominant material removing mechanism (MRM) is melting. Another approach consists of using a conductive layer referred as assisting electrode (AE) and was used on the surface of the workpiece to make it conductive.

In the current study, we investigated the machinability of zirconia-MWCNT using 1 wt % and 2 wt % CNT content. The composites showed high electrical conductivity and then a successful EDM machining. Moreover, the study of the surface integrity of the machined samples showed that melting/evaporation and spalling are the main MRM [98]. More details are found in Chapter 5.

2.5 Thermal conductivity

Carbon nanotubes have a high thermal conductivity due to the large phonon mean free path in the strong carbon sp^2 bond network of CNT walls. However, there is a relatively large data scatter in the literature for thermal conductivity values of CNTs at room temperature. The commonly reported values for the thermal conductivity of individual CNTs are ~3,000 W mK^{-1} for MWCNTs and ~3,500 W mK^{-1} for single-walled carbon nanotubes (SWCNTs) at room temperature [115].

Bakshi et al. [116] showed that the increase of CNTs dispersion quality induces an increase in the thermal conductivity of Al_2O_3 coatings with 4 wt% MWCNTs. Kumari et al. [117], reported that the thermal properties of Al_2O_3-CNT composites are highly dependent on the CNT content, bulk density, and SPS conditions. However, in both studies [116,117] , the maximum increase in thermal conductivity was not as high as expected regarding the thermal conductivity of CNT. Zhang et al. [118] studied the thermal conductivity of SPSed bulk CNT samples. They showed that CNT results in low thermal conductivity (4.2 W mK^{-1}) when they are sintered to bulk samples. The tube-tube interaction was the main reason behind the low thermal conductivity. Huang et al. [119] reported a decrease in thermal conductivity of $BaTiO_3$-CNT composites due to the interfacial thermal barrier between CNTs and $BaTiO_3$. It was reported that the addition of MWCNTs increases the thermal conductivity of silica-MWCNT composites [120]. Jiang and Gao [121] found that the thermal conductivity increases with increasing the amount of MWCNTs in TiN-MWCNT composites.

In the present work, the thermal conductivity of zirconia-MWCNTs sintered at two different temperatures 1350 °C and 1500 °C have been studied. To the best of our knowledge, there has not been any work on the thermal conductivity of 3Y-TZP/CNT before. It was shown that the thermal conductivity of the studied composites (1 wt % CNT) sintered at 1350 °C is decreasing with increasing MWCNTs content, whereas only a small decrease in the composite with 1 wt % CNT content is observed at higher SPS temperature 1500 °C. The decrease of thermal conductivity with CNT content may be explained by the increase in porosity and the drop of elastic modulus [98].

CHAPTER 3

Materials and Methods

3.1 Materials

Commercially available yttria stabilized zirconia powder with 3 mol % yttria (TZ-3YSB-E, Tosoh Co, Japan) was used in the current study. The zirconia powder has a crystalline size of 30 nm and a particle size of 600 nm. The chemical composition of 3Y-TZP is illustrated in Table 3.1.

Table 3.1 Chemical composition of 3Y-TZP powder as given by the producer [122].

Elements	Composition in wt %
Y_2O_3	4.95-5.35
Al_2O_3	0.15-0.35
SiO_2	Max 0.02
Fe_2O_3	Max 0.01
NaO_2	Max 0.04

The as received 3Y-TZP powder, see Table 1, was heat treated at 750 °C in order to burn of the organic additives. The carbon nanotubes used to reinforced zirconia were MWCNT (Graphistrength C100) supplied from Arkema, France, with an outer diameter 10-15 nm, inner diameter 2-6 nm and length 0.1-10 μm (see Fig.3.1). The different amount of MWCNT contents chosen to reinforce zirconia were 0.5, 1 and 2 wt %.

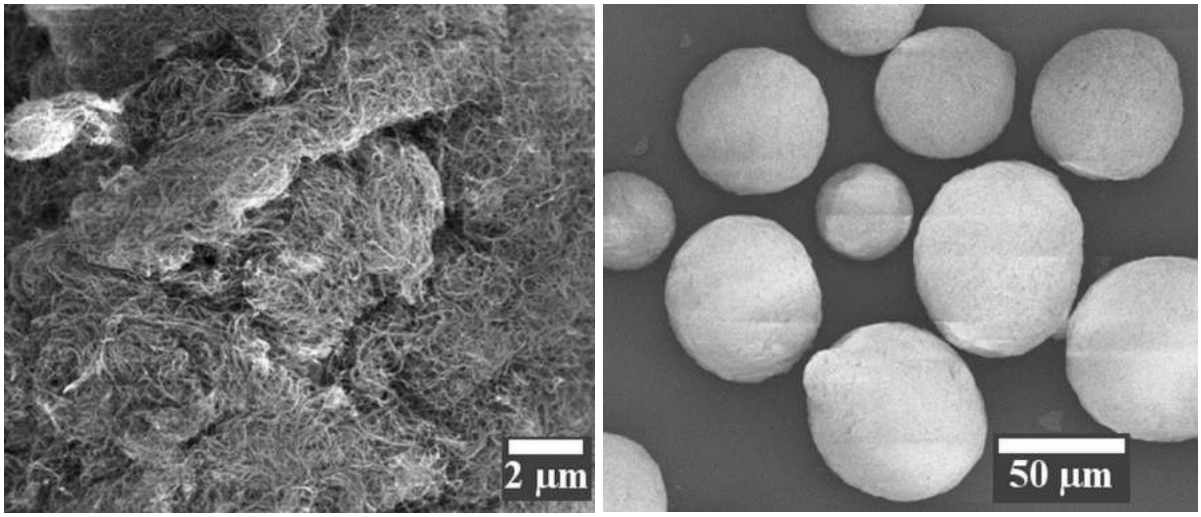

Fig.3.1 Shape of as received MWCNTs bundles and zirconia powder.

3.2 Powder processing and sintering

Multi-walled carbon nanotubes were initially dispersed in N, N dimethylformamid (DMF) using ultrasonication from 2 to 4 hours depending on the amount of MWCNT used. The heat treated zirconia powder was then added to the dispersed MWCNT-DMF solution. After that, the mixture was milled using a planetary ball milling for 4 hours running at a velocity of 300 rpm using a mixture of different sized zirconia balls of diameter 10, 5 and 3 mm. The milled slurry was then dried at 70 °C for 24 hours. Finally, the powder-fibre mixture was passed through sieve of 250 μm.

Another method of the composite powder processing was used in order to improve the dispersion of CNT within zirconia matrix. The processing method consists of dry mixing MWCNTs together with zirconia powder using "Turbula" mixer for 24 hours. However, the dry powder processing method was not as successful as the first method which consists of using DMF as a dispersant.

Sintering is the next step after powder processing. The composite powder was sintered using Spark Plasma Sintering HPD 25/1 (FCT System, Germany) furnace at Queen Mary college, London, UK. SPS allows sintering to fully dense composites at lower temperatures and at shorter holding times compared with normal sintering, which preserves CNTs against damage as reported in section 1.3.2.

The powder-fibre was filled into a graphite die and then heated with a heating rate of 100 °C/min to the holding temperature of 1350 °C. An axial pressure of 50 MPa was applied at 1350 °C for a dwell time of 5 min and then cooled down at a rate of 100 °C /min. After the sintering procedure, the final samples had a shape of flat discs with 3 mm thickness and a diameter of 40 mm and 50 mm. The samples were then polished using series of steps of diamond suspensions from 30 μm down to 3 μm before a final polishing step with colloidal silica was made. The samples were then thermally etched

in air at 1100 °C with a dwell time of 1 hour in order to reveal grain sizes and microstructure. The average grain size of each composite was determined using the line intercept method on scanning electron microscopy (SEM) images.

3.3 Microstructural analysis

3.3.1 Density

The bulk density of 3Y-TZP/CNT composites was determined using Archimedes method. Since there was no reaction between CNTs and 3Y-TZP matrix, the theoretical density of the composites was calculated according to the rule of mixtures. The theoretical density of zirconia is 6.1 $g \cdot cm^{-3}$. However, the exact density of MWNTs is not known because it depends on their purity, number of walls and external diameter. Therefore, the value 1.8 $g \cdot cm^{-3}$ was considered for the density of CNTs based on literature data [123].

3.3.2 Confocal microscope

A laser confocal microscope (Olympus, LEXT OLS 3100) was used to characterize the Vickers indentations by measuring the crack lengths and the diagonal lengths of the imprints.

3.3.3 Scanning Electron Microscope (SEM)

A Scanning Electron Microscope (JEOL JSM 6400) and a high resolution scanning electron microscope (Magellan 400, FEI Company) were used for initial microstructural characterization such as grain size measurements, the analysis of CNTs dispersion and fractography examinations. The sample surfaces were coated with a thin layer of carbon before introducing the samples in the SEM chamber to improve the electric conductivity of the sample surface for a better imaging of surface structures in the SEM.

3.3.4 Focused Ion Beam (FIB)

Focus ion beam (FIB) operates in a similar way as the SEM. Both systems used focused beam to create a specimen image, ion beam for the FIB, an electron beam for the SEM. A reservoir of gallium (Ga) is positioned in contact with a sharp Tungsten (W) needle. A high extraction field is used to pull the liquid Ga into a sharp cone whose radius may be 5–10 nm. Ions are emitted and then accelerated down the FIB column. The reasons behind the use of Ga are that Ga has a melting temperature of only 30 °C, thus, it exists

in the liquid state near room temperature. Moreover, Ga ions can be focused to a very small probe area of only 10 nm in diameter.

The Ga^+ ion beam is focused onto the area of interest on the surface. Once the beam hits the surface it enters the sample and creates cascade of events which results in the ejection of sputtered particles in the form of ions that leave the surface as secondary ions (i^+ or i^-) or neutral atoms (n^0), as well as secondary electrons (e^-), see Fig 3.2.The electron beam is used to raster the surface while the signals from the emitting ions are used to form the image. The primary ion penetration depth is approximately 20 nm for 25 keV Ga^+. The high beam currents are used for milling large areas quite rapidly, and low beam currents are used for polishing the milled surface before imaging. FIBs typically operate with an accelerating voltage between 5 and 50 keV [124].

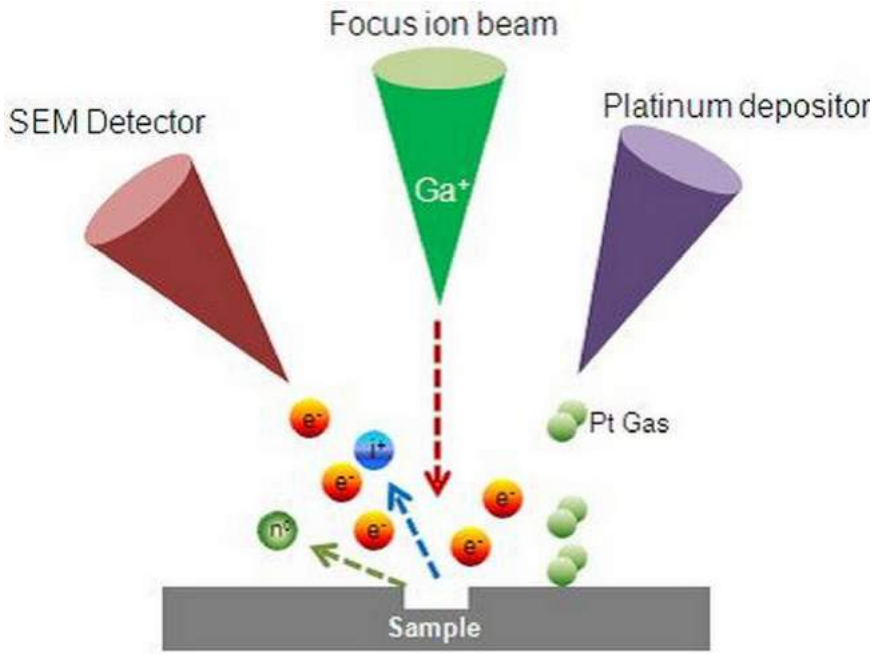

Fig.3.2 Principle of FIB imaging.

In this thesis a dual beam focused ion beam (FIB) /SEM Microscope (Zeiss Neon 40) was used mainly to investigating the subsurface damage below nanoindentation and in front of the notch tip induced by laser ablation. A thin platinum layer was deposited on the sample prior to FIB machining in order to minimize ion-beam damage. A Ga^+ ion source was used to mill the surface at a voltage of 30 kV. The final polishing of the cross-sections was performed at 10 pA.

3.4 Phase characterization

3.4.1 X-Ray Diffraction (XRD)

The X-ray diffraction (XRD) was used to identify the crystallographic phases with Bragg-Brentano symmetric-geometry, using PANalytical Empyrean equipment with PIXcel-3D detector and Cu-K_α 45 kV and 30 mA radiation. The XRD spectra were obtained in a scan range of 20 ° ≤2 θ ≤ 100 °, using a step size of 0.013 ° and an anti-scatter slit of 1 °. The monoclinic volume fraction, V_m, content was calculated by the equation proposed by Toraya et al. [125],

$$V_m = \frac{1.311 \times (I_m^{(\bar{1}11)} + I_m^{(111)})}{1.311 \times \left(I_m^{(\bar{1}11)} + I_m^{(111)}\right) + I_t^{(111)}} \tag{3.1}$$

where $I_m^{(hkl)}$and $I_t^{(hkl)}$represent the intensities of the (hkl) peak of the monoclinic and tetragonal phases, respectively.

3.4.2 Raman spectroscopy

In the current study, Raman spectroscopy (alpha300RA+ from WITec GmbH) was used at Universitat de Barcelona (UB) to analyse the effect of MWCNTs on the tribological properties of the composites where signals from both inside and outside the wear tracks were compared. Raman spectra were recorded using the 532 nm laser wavelength excitation and an acquisition range from 100 to 3000 cm^{-1}.

3.5 Mechanical testing

3.5.1 Hardness and indentation fracture toughness

Vickers indenter was used to indent the specimen´s surface inducing cracks at the corners of the residual indentation impressions. The crack lengths and the imprint area were then measured to determine the Vickers hardness (HV) and the indentation fracture toughness.

Taking into account the Palmqvist morphology of the indentation cracks, the expression proposed by Niihara [73] for Palmqvist cracks is the most appropriate for determining the indentation fracture toughness, see Fig.3.3. Anstis et al. [72] equation for median cracks was also used to compare the present results with other published results as well as to compare the resistance to cracking by a Vickers indenter of composites with different amounts of CNTs. Moreover, in the literature, the equation

for fracture toughness of median radial cracks is often employed independently of the shape of the cracks.

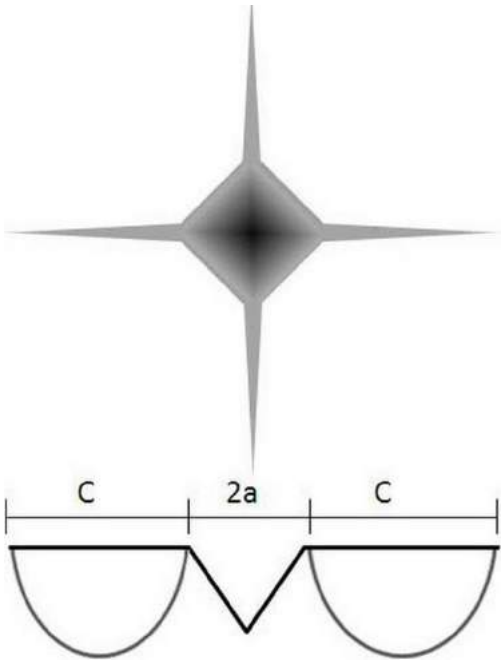

Fig.3.3 Vickers indentation with Palmqvist cracks.

Vickers Hardness of the material is given by the following equation:

$$H_v = 1.854\frac{P}{2a^2} \tag{3.2}$$

Fracture toughness K_{Ic} using the equation of Niihara et al [73]

$$K_{IC} = 0.018H\sqrt{a}\left(\frac{E}{H}\right)^{0.4}\left(\frac{c}{a}-1\right)^{0.5} \tag{3.3}$$

Fracture toughness using Anstis et al equation [72]

$$K_{IC} = 0.016\left(\frac{E}{H}\right)^{0.5}\left(\frac{P}{c^{3/2}}\right) \tag{3.4}$$

where c refers to the crack length and E is the elastic modulus and H is the hardness calculated from the indentation load P and the projected area of the imprint as follows:

$$H = \frac{P}{2a^2} \tag{3.5}$$

Indentation fracture toughness does not measure the true fracture toughness but rather the resistance to cracking by sharp contact loading as it was well explained in section 2.1.1. Therefore, in the current study, a new method is developed for the determination of the "true" fracture toughness of the nanocomposites.

3.5.2 True fracture toughness

The method is based on inducing a sharp shallow notch on the surface of a prismatic bar by means of a femtolaser. The femtolaser system used to produce the notch was a commercial Ti: Sapphire oscillator (Tsunami, Spectra Physics) and a regenerative amplifier system (Spitfire, Spectra Physics) based on chirped pulsed amplification. The femtolaser delivered 120 fs linearly polarized pulses at 795 nm wave length with a repetition rate of 1 kHz. The pulse energy used was 5 mJ and the focusing system was an achromatic doublet lens with 50 mm focal length. The samples were placed on a XYZ motorized stage and moved along one of the horizontal axis with a scanning speed of 50 μm/s. Four passes were needed to achieve the desired notch depth (~ 24 μm).

The stress intensity factor, K_I, was obtained by using the following expressions proposed by Munz and Fett [126]:

$$K_I = \frac{3F(S_1 - S_2)}{2BW^2} Y\sqrt{a} \tag{3.6}$$

$$Y = \frac{1.1215\sqrt{\pi}}{\beta^{3/2}}\left[\frac{5}{8} - \frac{5}{12}\alpha + \frac{1}{8}\alpha^2\beta^6 + \frac{3}{8}exp\left(-\frac{6.1342\alpha}{\beta}\right)\right] \tag{3.7}$$

where $S_1$and S_2 are the outer and inner spans respectively, B is the thickness, W the width, F the applied load, a is the crack length, which is taken as the depth of the notch plus the small damage region in front of the notch, $\alpha = a/W$ and $\beta = 1 - \alpha$.

The tests were performed for the composites with 0, 0.5 and 2 wt % CNT content. Additional tests were carried out in standard 3Y-TZP with larger grain size (~330 nm). Finally, the notched bar specimens (4 mm x 2.5 mm x 40 mm) were tested in a four point bending test device (DEBEN, Microtest, UK) in air with spans of 30/12 mm. The average stress rate was 2.4 MPa/s. Three specimens were used for each composition.

3.5.3 Nanoindentation

Instrumented indentation is a technique in which an indenter is applied on the surface and both the applied load and the measured displacement are recorded simultaneously throughout the experiment. When the applied displacements and loads are very low the instrumented indentation technique is often referred to as nanoindentation. It is used for the determination of the near surface mechanical properties such as elastic modulus and hardness, among many other applications such as in thin films. The most used method to extract the mechanical properties is the one introduced by Olivier and Pharr in 1992 [127]. The experiment set up requires a sample with a flat surface and an indenter usually made of diamond that penetrates perpendicularly into the surface. The depth of penetration at a given load is a response to the material´s resistance to deformation. The most commonly used indenter geometry is Berkovich geometry which consists of three sided pyramid with an opening angle of 142.3 ° between one edge and the opposing face of the indenter. Depth from nanometres to millimetres can be covered to determine materials properties over a large or a local volume at the nanoscale. "Nanoscale" has been defined by the ISO standard ISO14577 as 0–200 nm in penetration depth, "microscale" from 200 nm to an applied force of 2 N, and "macroscale" for forces larger than 2 N (ISO-14577-1 2002) [128].

The measured parameters during nanoindentation test are the applied load (P), the total displacement relative to the initial undeformed surface (h), the contact depth (h_c), the final depth (h_f), and the contact stiffness $S = dP/dh$. The contact stiffness is defined as the slope of the upper portion of the unloading curve during the initial stages of unloading, see also Fig.3.4.

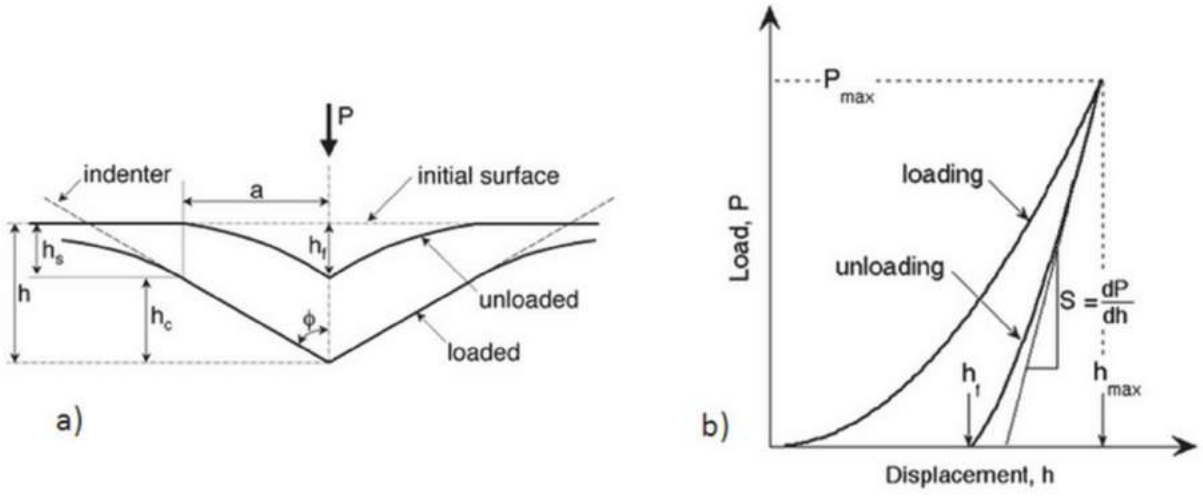

Fig.3.4 Schematic of the a) unloading process showing the contact geometry and b) load-displacement curve [127].

The contact depth is estimated from the load-displacement data using the following equation:

$$h_c = h_{max} - \varepsilon\left(\frac{P_{max}}{S}\right) \tag{3.8}$$

where P_{max} is the peak indentation load and ε is a constant which equal to 0.75 for a Berkovich indenter [128].
The projected area A is estimated by evaluating the indenter shape function at the contact depth h_c, $A = f(h_c)$. Then the hardness H and the effective elastic modulus E_{eff} are calculated as follows:

$$S = \beta\frac{2}{\pi}\,E_{eff}\,\sqrt{A}H = \frac{P_{max}}{A} \tag{3.9}$$

where β is a constant equal to 1.034 in the case of a Berkovich indenter.

$$\frac{1}{E_{eff}} = \frac{1-\nu^2}{E} + \frac{1-{\nu_i}^2}{E_i} \tag{3.10}$$

The effective elastic modulus, E_{eff}, takes into account the fact that elastic displacements occur in both the specimen with Young´s modulus E and Poisson´s ratio ν, and the indenter with E_i and ν_i.

In this thesis, nanoindentation tests were performed using a Nanoindenter XP from Agilent Technologies equipped with continuous stiffness measurements (harmonic displacement 2 nm and frequency of 45 Hz), using a pyramidal Berkovich diamond indenter. The strain rate was held constant at 0.05 s^{-1}. The nanoindentation curves were analysed using the Oliver and Pharr method [127] in order to measure the nanoindentation hardness (H_{Berk}) and the elastic modulus (E_{Berk}) as a function of the penetration depth for each composition where H_{Berk} was defined as the ratio of load and contact area at maximum load. The indenter shape was carefully calibrated for true penetration depths as small as 50 nm by indenting fused silica samples of well-known Young's modulus (72 GPa). The indents were organized in a regularly spaced array of 25 indentations (5 by 5) at a maximum penetration depth of 2000 nm or until reaching the maximum applied load, 650 mN. Each indentation was performed with a spacing distance of 50 μm in order to avoid any overlapping effect.

3.6 Tribological characterization

3.6.1 Scratch testing

The scratch test can be carried out under a constant load and an incremental load. During scratch testing a stylus is moved over a specimen surface with a linearly increasing load until failure occurs at critical load L_c, and the normal force F_z and the tangential force F_x are recorded. Acoustic Emission (AE) is also measured. An optical microscope is used to evaluate the damage induced after scratch testing, see Fig 3.5.

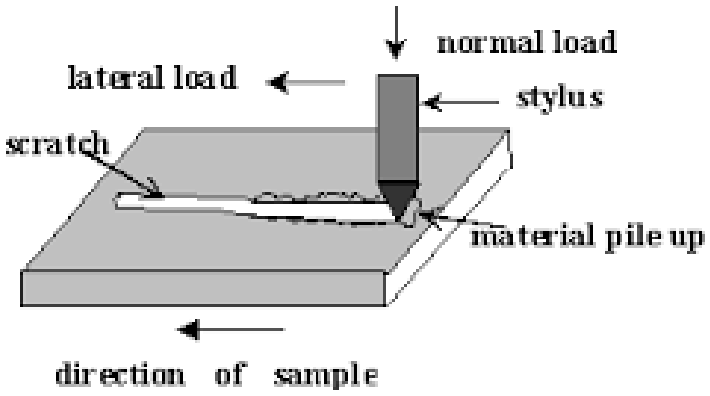

Fig.3.5 Schematic showing the different parameters involved during scratch test [129].

In the current study, nano-scratch tests were carried out with a nano-scratch attachment of the Nanoindenter XP that allows lateral force measurements. A Berkovich indenter was employed to scratch the surface under increasing load at a velocity of 10 μm/s for a total scratch length of 500 μm up to a maximum load of 40 mN. Three different scratches were performed on each sample. Lateral (friction) forces were calculated from the deflection of the loading column. The coefficient of friction (COF) was determined by taking the ratio of the lateral force measured by the equipment and the normal load applied on the material.
Macro-scratch testing was conducted using a sliding Rockwell indenter with a diamond spherical tip radius of 200 μm (automatic Scratch Tester, CSM-Instruments, Switzerland). Both normal and tangential forces were recorded. Applied load ranged from 1 to 150 N over a sliding distance of 7.5 mm at a sliding speed 5 mm/min.

3.6.2 Wear test

Tribology tests were performed on an automatic tribometer (Wazau TRM1000, Germany) in reciprocating dry sliding conditions, using ball on disc geometry, at ambient temperature and pressure. A zirconia ball with 10 mm diameter was used as a

counterpart. All the tests were carried out under a constant normal load of 5 N, a sliding velocity of 300 rpm and a stroke length of 4 mm. The total sliding distance was 100 m. At least four tests were performed for each condition and data represent their average. The COF was calculated by taking the ratio of the tangential and normal forces and it was reported versus the sliding distance. The volume removed was measured using a stylus profilometer where a hundred profiles along the width of the track were recorded. The wear rate, W, was determined in terms of the volume loss V per distance L and applied load F according to the following equation:

$$W = \frac{V}{L \cdot F} \tag{3.11}$$

3.7 Electrical conductivity and Electrical Discharge machining (EDM) characterization

In the current work, the electrical conductivities of all composites were measured by four-point method. A direct current runs through the sample through outer Pt current leads and the resistivity of the sample is measured using two "inner" Ni Voltage probes. The measurement was done with an accurate digital micro-ohmmeter (Keithley 580) using the four-point method on bar-shaped specimens (4 mm x 4 mm x 18 mm) prepared using a diamond cutting machine. The conductivity of the material is calculated from the current, the measured voltage and the geometry of the arrangement.

Die sinking EDM ("*+GF+ AgieCharmilles"*) was carried out with 3Y-TZP/ 1 wt% CNT and 3Y-TZP/ 2 wt% CNTs composites as workpiece. The tool used was a copper tool electrode with a surface of 0.12 cm². The average observed current was 0.5 A and the overall machining distance was set to a value of $z = -0.2\,mm$ without rotation or planetary movement of the tool. The dielectric used lubricating oil named "IonoPlus IME-MH".

To achieve a surface roughness of R_a=0.1, first impulse set 1 and afterwards impulse set 2 of the machine were used to machine the material under the boundary condition "Cu – Carbide Metal". The composites subjected to EDM were in the shape of one quadrant of the sintered discs, clamped by the sides and machined on one diametric plane.

3.8 Thermal conductivity characterization

In the present thesis, the thermal conductivity (K) was calculated in the composites with 0.5, 1 and 4 wt % CNT by measuring the thermal diffusivity (α), the density (ρ)

and the specific heat capacity (C_p), for a temperature range of 25-950 °C, according to the equation below:

$$K = \alpha \times \rho \times C_p \quad (3.12)$$

The thermal diffusivity was determined by laser-flash method (Laser Flash Apparatus, Netzsch LFA 457, Germany) where disk-shaped specimens were thin coated with graphite, ASTM E2585-09 (2009) [130]. The specific heat capacity was measured under argon atmosphere using a differential scanning calorimeter (Netzsch DSC 404C, Germany). The measurements were carried out in Technical University of Denmark (DTU).

CHAPTER 4

Conclusions and Future work

4.1 Conclusions

The processing and the properties of zirconia-MWCNT have been studied and the following conclusions can be made:

1. The use of SPS for sintering zirconia and zirconia-MWCNT composites results in high density ceramics with smaller grain size than those produced under conventional conditions by compacting and sintering. The addition of MWCNT decreases further the grain size. As the concentration of MWCNT increases above 0.5 % MWCNT, no full density is achieved and hardness and elastic modulus decrease.

2. The friction coefficient extracted from nano-scratch and wear tests decreases with the addition of MWCNTs. In macro-scratch tests using higher loads, there is a critical load over which the friction coefficient increases with CNT addition and brittle fracture starts. The low friction coefficient is attributed to the formation of a carbon tribo-film during reciprocation sliding.

3. A novel method for the calculation of the "true" fracture toughness of small cracks is successfully established. A very sharp notch in the scale of a few tens of microns and sub-micrometer tip radius less than 0.5 μm was induced in zirconia-MWCNT composite using Ultra-short Pulsed Laser Ablation (UPLA).

4. The "true" fracture toughness of zirconia and zirconia-MWCNT for small cracks is found to be low and practically independent of the CNT amount. Vickers indentation fracture toughness is higher and increases with increasing CNT. In this way it is shown that indentation fracture toughness is not an appropriate method for analysing the influence of MWCNT on true fracture toughness. Even in the absence of MWCNT,

the fracture toughness of SPS zirconia measured from small surface cracks induced by UPLA is found to be lower than measured by conventional fracture toughness methods with long cracks. The increase observed in indentation fracture toughness with the addition of MWCNT is attributed to an increase in the resistance to cracking under sharp contact loading because of change in the elasto-plastic behaviour induced by the addition of MWCNT.

5. The addition of MWCNTs strongly increases the electrical conductivity of the studied composites. While, the thermal conductivity increases slightly with increasing CNT content and SPS temperature.

6. The composites with 1 wt % and 2 wt % MWCNT content can successfully be machined using EDM due to their high electrical conductivity. The material removal mechanism is found to be melting/evaporation and spalling.

7. A study of the effect of grinding on the SPS zirconia samples with a wide range of grain sizes shows that a thermal etching of ground zirconia at 1100 °C for 1 hour in air induces a nano-grain layer with grains of about 60 nm and a thickness of less than a few hundred nanometers, which is independent of the original grain size. At much higher temperature, 1575 °C for 1 hour, thermal etching of ground or polished zirconia induces similar grain size.

8. The influence of transformation toughening in the behaviour of small cracks was also conducted in conventionally sintered 12Ce-ZrO_2 (300 nm grain size) because it has much higher plateau fracture toughness than 3Y-TZP (177 nm grain size). By inducing a similar short sharp notch using UPLA in both materials, the difference in strength is only about 10%. This means that the true fracture toughness difference for these small cracks is also less than about 10 % in comparison with plateau values of fracture toughness which are different by a factor ≈3. Therefore, the beneficial effect of higher indentation fracture toughness in 12Ce-ZrO_2 reported in literature has a very small effect on the real effective fracture toughness that determines the strength of unshielded small cracks.

4.2 Future work

1. Dispersion is a crucial step in the processing of zirconia-CNT composites. Different dispersion solvents of CNTs should be studied and an optimized method for dispersion of MWCNTs in ceramic matrix composites should be established. Interfacial bonding should be improved by coating zirconia with functionalised CNTs for example.

Homogeneous dispersion and interfacial bonding may increase the mechanical properties.

2. The addition of CNT up to 4 wt % results in high electrical conductivity, reported for the first time, in zirconia-MWCNT composites. It would be interesting to investigate the potential of using higher CNT content and high temperatures on the electrical conductivity and on the machining of the composites.

3. CNTs are in the nanoscale and they are located in the grain boundaries on zirconia matrix. Oxidizing CNTs leaves a porous nanoscale network in zirconia matrix. It would be of great interest to use CNTs to produce porous ceramic materials with nanosized long channels.

4. Since the thermal etching after grinding SPSed zirconia results in nanograin layer with few hundred nanometers in thickness independently of the bulk grain size, a study of LTD resistance of thermal etched ground zirconia samples with large bulk grain size could be interesting in order to see if this nano-layer protects large bulk grain size zirconia from LTD.

5. The use of SPS allows sintering the studied composites in short time and low temperature which results in small grain size. An alternative methods as Hot Isostatic Pressing (HIP) could be also used to compare with SPS and gain deeper understanding of the sintering mechanism.

REFERENCES

[1] J. Chevalier, L. Gremillard, S. Deville, Low-Temperature Degradation of Zirconia and Implications for Biomedical Implants, Annu. Rev. Mater. Res. 37 (2007) 1-32.

[2] P. Li, I.-W. Chen, J.E. Penner-Hahn, Effect of Dopants on Zirconia Stabilization-An X-ray Absorption Study: I, Trivalent Dopants, J. Am. Ceram. Soc. 77 (1994) 118–128.

[3] J. Chevalier, L. Gremillard, A. V. Virkar, D.R. Clarke, The Tetragonal-Monoclinic Transformation in Zirconia: Lessons Learned and Future Trends, J. Am. Ceram. Soc. 92 (2009) 1901–1920.

[4] R.H.J. Hannink, P.M. Kelly, B.C. Muddle, Transformation Toughening in Zirconia-Containing Ceramics, J. Am. Ceram. Soc. 83 (2004) 461–487.

[5] P.M. Kelly, L.R.F. Rose, The martensitic transformation in ceramics and its role in transformation toughening, J. Am. Ceram. Soc. 47 (2002) 463–557.

[6] F.F. Lange, Transformation toughening, J. Mater. Sci. 17 (1982) 225–234.

[7] R.M. McMeeking, A.G. Evans, Mechanics of Transformation-Toughening in Brittle Materials, J. Am. Ceram. Soc. 65 (1982) 242–246.

[8] P. Palmero, Structural Ceramic Nanocomposites: A Review of Properties and Powders Synthesis Methods, Nanomaterials. 5 (2015) 656–696.

[9] A. V. Virkar, R.L.K. Matsumoto, Ferroelastic Domain Switching as a Toughening Mechanism in Tetragonal Zirconia, J. Am. Ceram. Soc. 69 (1986) C–224–C–226.

[10] R.H.J. Hannink, P.M. Kelly, B.C. Muddle, Transformation Toughening in Zirconia Containing Ceramics, J. Am. Ceram. Soc. 83 (2004) 461–487.

[11] H. Fischer, W. Rentzsch, R. Marx, R-Curve Behaviour of Dental Ceramic, J. Dent. Res. (2002) 547–551.

[12] R.O. Ritchie, Mechanisms of fatigue crack propagation in metals, ceramics and composites: Role of crack tip shielding, Mater. Sci. Eng. A. 103 (1988) 15–28.

[13] J. Eichler, M. Hoffman, U. Eisele, S. Rul, R-curve behaviour of 2Y-TZP with submicron grain size, J. Eur. Ceram. Soc. 26 (2006) 3575–3582.

[14] N. Gupta, P. Mallik, B. Basu, Y-TZP ceramics with optimized toughness : new results, J. Alloy. Compd. 379 (2004) 228–232.

[15] G. Fargas, D. Casellas, L. Llanes, M. Anglada, Thermal shock resistance of yttria-stabilized zirconia with Palmqvist indentation cracks, J. Eur. Ceram. Soc. 23 (2003) 107–114.

[16] H. Hobner, Sub-critical crack extension and crack resistance in polycrystalline alumina, Mater. Sci. 12 (1977) 117–125.

[17] D. Munz, What can we learn from R-curve measurements, J. Am. Ceram. Soc. 90 (2007) 1–15.

[18] K. Kobayashi, H. Kuwajima, T. Masaki, Phase change and mechanical properties of ZrO_2-Y_2O_3 solid electrolyte after ageing, Solid State Ionics 4 (1981) 489–493.

[19] R.L.K. Matsumoto, Strength Recovery in Degraded Yttria-Doped Tetragonal Zirconia Polycrystals, J. Am. Ceram. Sci. 213 (1985) 1984–1986.

[20] E.M. Santos, S. Vohra, S.A. Catledge, M.D. Mcclenny, J. Lemons, K.D. Moore, Examination of Surface and Material Properties of Explanted Zirconia Femoral Heads, J. Arthroplasty. 19 (2004) 30–34.

[21] M. Yoshimura, T. Noma, K. Kawabata, S. Somiya, Role of H_2O on the degradation process of Y-TZP, J. Mater. Sci. Lett. 6 (2000) 465–467.

[22] J. Chevalier, B. Cales, J.M. Drouin, Low-Temperature Aging of Y-TZP Ceramics, J. Am. Ceram. Sci. 54 (1999) 2150–2154.

[23] J. Chevalier, What future for zirconia as a biomaterial, Biomaterials. 27 (2006) 535–543.

[24] E. Djurado, L. Dessemond, C. Roux, Phase stability of nanostructured tetragonal zirconia Polycrystals versus temperature and water vapour, Solid State Ionics 137 (2000) 1249–1254.

[25] R. Chintapalli, A. Mestra, F. García Marro, H. Yan, M. Reece, M. Anglada, Stability of Nanocrystalline Spark Plasma Sintered 3Y-TZP, Materials 3 (2010) 800–814.

[26] A. Paul, B. Vaidhyanathan, J.G.P. Binner, Hydrothermal Aging Behaviour of Nanocrystalline Y-TZP Ceramics, J. Am. Ceram. Sci. 2152 (2011) 2146–2152.

[27] L. Ruiz, M.J. Readey, Effect of heat treatment on grain size, phase assemblage and mechanical properties of 3 mol % Y-TZP, J. Am. Ceram. Sci. 79 (1996) 2331-2340.

[28] K. Matsui, H. Horikoshi, N. Ohmichi, M. Ohgai, H. Yoshida, Y. Lkuhara, Cubic-Formation and Grain-Growth Mechanisms in Tetragonal Zirconia Polycrystal, J. Am. Ceram. Sci. 8 (2003) 1401–1408.

[29] S. Deville, M. Etienne, R. Jullian, Critical effect of cubic phase on aging in 3 mol % yttria-stabilized zirconia ceramics for hip replacement prosthesis, 25 (2004) 5539–5545.

[30] S. Schmauder, H. Schubert, Significance of Internal Stresses for the Martensitic Transformation in Yttria-Stabilized Tetragonal Zirconia Polycrystals during Degradation, J. Am. Ceram. Sci. 69 (1985) 534–540.

[31] J.F. Jue, J. Chen, A. V Virkar, low-Temperature aging of t'-Zirconia: The Role of Microstructure, J. Am. Ceram. 20 (1991) 1811–1820.

[32] M. Guazzato, M. Albakry, S.P. Ringer, M. V Swain, Strength, fracture toughness and microstructure of a selection of all-ceramic materials. Part II. Zirconia-based dental ceramics, Dent. Mat. (2010) 449–456.

[33] I. Denry, J.R. Kelly, State of the art of zirconia for dental applications, Dent. Mat. 4 (2007) 299–307.

[34] W. Krätschmer, L.D. Lamb, K. Fostiropoulos, D.R. Huffman, Solid C60: a new form of carbon, Nature. 347 (1990) 354–358.

[35] S. Iijima, Helical microtubules of graphitic carbon, Nature. 354 (1991) 56–58.

[36] S. Iijima, T. Ichihashi, Single-shell carbon nanotubes of 1 nm diameter, Nature. 363 (1993) 603–605.

[37] F. Inam, Development of Ceramic-Carbon Nanotube (CNT) Nanocomposites, PhD thesis submitted to School of Engineering and Materials Science Queen Mary, University of London, 2009.

[38] Y. Saito, Carbon Nanotube and Related Field Emitters, Wiley-VCH Verlag GmbH & Co. KGaA, Weinheim, Germany, 2010.

[39] E.T. Thostenson, Z. Ren, T.-W. Chou, Advances in the science and technology of carbon nanotubes and their composites: a review, Compos. Sci. Technol. 61 (2001) 1899–1912.

[40] X. Zhao, M. Ohkohchi, M. Wang, S. Iijima, T. Ichihashi, Y. Ando, Preparation of high-grade carbon nanotubes by hydrogen arc discharge, Carbon N. Y. 35 (1997) 775–781.

[41] X. Zhao, M. Wang, M. Ohkohchi, Y. Ando, Morphology of Carbon Nanotubes Prepared by Carbon Arc, J. Appl. Phys. 35 (1996) 4451–4456.

[42] M. Wang, X. Zhao, M. Ohkohchi, Y. Ando, Carbon Nanotubes Grown on the Surface of Cathode Deposit by Arc Discharge, Fullerene. Sci. Tech. 4 (1996) 1027–1039.

[43] D.S. Bethune, C.H. Klang, M.S. de Vries, G. Gorman, R. Savoy, J. Vazquez, et al., Cobalt-catalysed growth of carbon nanotubes with single-atomic-layer walls, Nature. 363 (1993) 605–607.

[44] Y. Saito, M. Okuda, N. Fujimoto, T. Yoshikawa, M. Tomita, T. Hayashi, Single-Wall Carbon Nanotubes Growing Radially from Ni Fine Particles Formed by Arc Evaporation, J. Appl. Phys. 33 (1994) L526–L529.

[45] Y. Saito, K. Nishikubo, K. Kawabata, T. Matsumoto, Carbon nanocapsules and single-layered nanotubes produced with platinum-group metals (Ru, Rh, Pd, Os, Ir, Pt) by arc discharge, J. Appl. Phys. 80 (1996) 3062.

[46] B. Chen, X. Zhao, S. Inoue, Y. Ando, Fabrication and Dispersion Evaluation of Single-Wall Carbon Nanotubes Produced by FH-Arc Discharge Method, J. Nanosci. Nanotechnol. 10 (2010) 3973–3977.

[47] J. Robertson, H. Kawarada, E. Kohn, R. Hamers, B. Chen, S. Inoue, et al., Raman spectroscopic and thermogravimetric studies of high-crystallinity SWNTs synthesized by FH-arc discharge method, Diam. Relat. Mater. 18 (2009) 975–978.

[48] W. Fan, J. Zhao, Y. Lv, W. Bao, X. Liu, Synthesis of SWNTs from charcoal by arc-discharging, J. Wuhan Univ. Technol. Sci. Ed. 25 (2010) 194–196.

[49] J. Prasek, J. Drbohlavova, J. Chomoucka, J. Hubalek, O. Jasek, V. Adam, et al., Methods for carbon nanotubes synthesis—review, J. Mater. Chem. 21 (2011) 15872.

[50] Y. Watanabe, T. Asano, H.Y. Chang, H. Fujiyama, R. Mc Williams, T. Watanabe, et al., Production of single-wall carbon nanotubes by a XeCl excimer laser ablation, Thin Solid Films. 506 (2006) 255–258.

[51] J. Robertson, N. Fotopoulos, J.P. Xanthakis, A molecular level model for the nucleation of a single-wall carbon nanotube cap over a transition metal catalytic particle, Diam. Relat. Mater. 19 (2010) 557–561.

[52] O. Lee, J. Jung, S. Doo, S.-S. Kim, T.H. Noh, K.-I. Kim, et al., Effects of temperature and catalysts on the synthesis of carbon nanotubes by chemical vapour deposition, Met. Mater. Int. 16 (2010) 663–667.

[53] A.S. Afolabi, A.S. Abdulkareem, S.D. Mhlanga, S.E. Iyuke, Synthesis and purification of bimetallic catalysed carbon nanotubes in a horizontal CVD reactor, J. Exp. Nanosci. 6 (2011) 248–262.

[54] S. Dumpala, J.B. Jasinski, G.U. Sumanasekera, M.K. Sunkara, Large area synthesis of conical carbon nanotube arrays on graphite and tungsten foil substrates, Carbon N. Y. 49 (2011) 2725–2734.

[55] E. Flahaut, C. Laurent, A. Peigney, Catalytic CVD synthesis of double and triple-walled carbon nanotubes by the control of the catalyst preparation, Carbon N. Y. 43 (2005) 375–383.

[56] S.C. Lyu, T.J. Lee, C.W. Yang, C.J. Lee, Synthesis and characterization of high-quality double-walled carbon nanotubes by catalytic decomposition of alcohol, Chem. Commun. (2003) 1404.

[57] H. Cui, G. Eres, J.Y. Howe, A. Puretkzy, M. Varela, D.B. Geohegan, et al., Growth behaviour of carbon nanotubes on multi-layered metal catalyst film in chemical vapour deposition, Chem. Phys. Lett. 374 (2003) 222–228.

[58] J. Hilding, E. a. Grulke, Z. George Zhang, F. Lockwood, Dispersion of Carbon Nanotubes in Liquids, J. Dispers. Sci. Technol. 24 (2003) 1–41.

[59] S. Tsang, Mechanical damage of carbon nanotubes by ultrasound, Carbon N. Y. 34 (1996) 814–816.

[60] K.B. Shelimov, R.O. Esenaliev, A.G. Rinzler, C.B. Huffman, R.E. Smalley, Purification of single-wall carbon nanotubes by ultrasonically assisted filtration, Chem. Phys. Lett. 282 (1998) 429–434.

[61] M.H. Bocanegra-Bernal, Hot isostatic pressing (HIP) technology and its applications to metals and ceramics, J. Mater. Sci. 39 (2004) 6399–6420.

[62] M. Koizumi, Hot Isostatic Pressing— Theory and Applications: Proceedings of the Third International Conference Osaka, Japan, 10-14 June 1991, Springer Science & Business Media, 2012.

[63] R. Schaefer, Hot isostatic pressing : theory and applications : proceedings of the Second International Conference, Gaithersburg, Maryland, USA, 7-9 June 1989, ASM International, Materials Park. Ohio, 1991.
[64] R. Tegman, Hot isostatic pressing of silicon nitride, Int. Ceram. 34 (1985) 22-28.
[65] R. Tegman, Hot Isostatic Pressing of Ceramic Waste Forms, Int. Ceram. (1985) 35–38.
[66] O. Guillon, J. Gonzalez-Julian, B. Dargatz, T. Kessel, G. Schierning, J. Räthel, M. Herrmann, Field-assisted sintering technology/spark plasma sintering: Mechanisms, materials, and technology developments, Adv. Eng. Mater. 16 (2014) 830–849.
[67] G. Bernard-Granger, N. Monchalin, C. Guizard, Comparisons of grain size-density trajectory during spark plasma sintering and hot-pressing of zirconia, Mater. Lett. 62 (2008) 4555–4558.
[68] J. Langer, M.J. Hoffmann, O. Guillon, Electric Field-Assisted Sintering in Comparison with the Hot Pressing of Yttria-Stabilized Zirconia, J. Am. Ceram. Soc. 94 (2011) 24–31.
[69] A.G. Evans, E.A. Charles, Fracture Toughness Determinations by Indentation, J. Am. Ceram. Soc. 59 (1976) 371–372.
[70] G.D. Quinn, R.C. Bradt, on the Vickers indentation fracture toughness Test, J. Am. Ceram. Soc. 90 (2007) 673–680.
[71] B.R. Lawn, A.G. Evans, D.B. Marshall, Elastic/Plastic Indentation Damage in Ceramics : The Median/Radial Crack System, J. Am. Ceram. Soc. 63 (1980) 574–581.
[72] G.R. Anstis, P. Chantikul, B.R. Lawn, D.B. Marshal, A critical evaluation of indentation techniques for measuring fracture toughness: I Direct crack measurements, J. Am. Ceram. Soc. 46 (1981) 533–538.
[73] K. Niihara, A fracture mechanics analysis of indentation-induced Palmqvist crack in ceramics, J. Mater. Sci. Lett. 2 (1983) 221–223.
[74] T. Konno, Physical Chem. Chang. Med. Mix. with Adsorbents Solid State. IV. Study Reduced-Pressure Mix. Pract. Use Amorph. Mix. Flufenamic Acid, Chem. Pharm. Bull. 38 (1990) 2003-2007.
[75] Z. Li, A. Ghosh, A.S. Kobayashi, R.C. Bradt, Indentation fracture toughness of sintered silicon carbide in the Palmqvist crack regime, J. Am. Ceram. Soc. 72 (1989) 904–911.
[76] C.B. Ponton, R.D. Rawlings, Vickers indentation fracture toughness test. Part 1. Review of literature and formulation of standardised indentation toughness equations, Mater. Sci. Technol. 5 (1989) 865–872.
[77] A. Ghosh, Z. Li, C.H. Henager, A.S. Kobayashi, R.C. Bradt, Vickers microindentation toughness of a sintered SiC in the median-crack regime, (1991) 1–33.

[78] L. Melk, J.J. Roa Rovira, F. García-Marro, M-L. Antti, B. Milsom, M.J. Reece, Nanoindentation and fracture toughness of nanostructured zirconia/multi-walled carbon nanotube composites, Ceram. Int. 41 (2015) 2453–2461.

[79] J.Y. Huang, S. Chen, Z.Q. Wang, K. Kempa, Y.M. Wang, S.H. Jo, G. Chen, M.S. Dresselhaus, Z.F. Ren, Superplastic carbon nanotubes, Nature. 439 (2006) 281.

[80] M.M.J. Treacy, T.W. Ebbesen, J.M. Gibson, Exceptionally high Young's modulus observed for individual carbon nanotubes, Nature. 381 (1996) 678–680.

[81] O. Lourie, D. Cox, H. Wagner, Buckling and Collapse of Embedded Carbon Nanotubes, Phys. Rev. Lett. 81 (1998) 1638–1641.

[82] G-D. Zhan, J.D. Kuntz, J. Wan, A.K. Mukherjee, Single-wall carbon nanotubes as attractive toughening agents in alumina-based nanocomposites, Nat. Mater. 2 (2003) 38–42.

[83] X. Wang, N.P. Pdture, H. Tanaka, Contact-damage-resistant ceramic/single-wall carbon nanotubes and ceramic/graphite composites, Nat. Mater. 3 (2004) 539–44.

[84] G.D. Quinn, R.C. Bradt, On the Vickers Indentation Fracture Toughness Test, J. Am. Ceram. Soc. 90 (2007) 673–680.

[85] J-W. An, D-H. You, D-S. Lim, Tribological properties of hot-pressed alumina–CNT composites, Wear. 255 (2003) 677–681.

[86] Z.H. Xia, J. Lou, W.A. Curtin, A multiscale experiment on the tribological behaviour of aligned carbon nanotube/ceramic composites, Scr. Mater. 58 (2008) 223–226.

[87] P. Hvizdoš, V. Puchý, A. Duszová, J. Dusza, Tribological behaviour of carbon nanofiber–zirconia composite, Scr. Mater. 63 (2010) 254–257.

[88] P. Hvizdoš, V. Puchý, A. Duszová, J. Dusza, C. Balázsi, Tribological and electrical properties of ceramic matrix composites with carbon nanotubes, Ceram. Int. 38 (2012) 5669–5676.

[89] A. Kasperski, A. Weibel, D. Alkattan, C. Estournès, V. Turq, C. Laurent, A. Peigney, Microhardness and friction coefficient of multi-walled carbon nanotube-yttria-stabilized ZrO_2 composites prepared by spark plasma sintering, Scr. Mater. 69 (2013) 338–341.

[90] L. Melk, J.J. Roa Rovira, M-L. Antti, M. Anglada, Coefficient of friction and wear resistance of zirconia–MWCNTs composites, Ceram. Int. 41 (2014) 459-468.

[91] L. Berhan, A.M. Sastry, Modeling percolation in high-aspect-ratio fiber systems. I. Soft-core versus hard-core models, Phys. Rev. E - Stat. Nonlinear, Soft. Matter. Phys. 75 (2007) 1–8.

[92] J.I.G. Ping Sheng, E.K. Sichel, Fluctuation-Induced Tunneling Conduction in Carbon-Polyvinylchloride, Phys. Rev. Lett. 40 (1981) 2–5.

[93] F.C. Fonseca, R. Muccillo, D.Z. De Florio, L.O. Ladeira, A.S. Ferlauto, Mixed ionic-electronic conductivity in yttria-stabilized zirconia/carbon nanotube composites, Appl. Phys. Lett. 91 (2007) 2007–2009.

[94] N. Song, H. Liu, Y.T. Yuan, J.Z. Fang, Fabrication and Characterization of SiC-Coated Multi-Walled Carbon Nanotubes Reinforced Reaction Bonded SiC Composite, Adv. Mater. Res. 936 (2014) 176–180.

[95] K. Ahmad, W. Pan, S-L. Shi, Electrical conductivity and dielectric properties of multiwalled carbon nanotube and alumina composites, Appl. Phys. Lett. 89 (2006) 133122.

[96] F. Inam, H. Yan, D.D. Jayaseelan, T. Peijs, M.J. Reece, Electrically conductive alumina–carbon nanocomposites prepared by Spark Plasma Sintering, J. Eur. Ceram. Soc. 30 (2010) 153–157.

[97] T. Ukai, T. Sekino, A.T. Hirvonen, N. Tanaka, T. Kusunose, T. Nakayama, K. Niihara, Preparation and Electrical Properties of Carbon Nanotubes Dispersed Zirconia Nanocomposites, Key. Eng. Mater. 317-318 (2006) 661–664.

[98] L. Melk, M-L. Antti, M. Anglada, Material removal mechanisms by EDM of zirconia reinforced MWCNT nanocomposites, Ceram. Int. (2016) 1–10. 5762-5801.

[99] I. Birkby, R. Stevens, Applications of Zirconia Ceramics, Key. Eng. Mater. 122-124 (1996) 527–552.

[100] O. Malek, J. Vleugels, Y. Perez, P. De Baets, J. Liu, S. Van den Berghe, B. Lauwers, Electrical discharge machining of ZrO_2 toughened WC composites, Mater. Chem. Phys. 123 (2010) 114–120.

[101] K. Ho, S. Newman, State of the art electrical discharge machining (EDM), Int. J. Mach. Tools Manuf. 43 (2003) 1287–1300.

[102] M. Kunieda, B. Lauwers, K.P. Rajurkar, B.M. Schumacher, Advancing EDM through Fundamental Insight into the Process, CIRP Ann. Manuf. Technol. 54 (2005) 64–87.

[103] H.C. Tsai, B.H. Yan, F.Y. Huang, EDM performance of Cr/Cu-based composite electrodes, Int. J. Mach. Tools Manuf. 43 (2003) 245–252.

[104] A. Banu, M.Y. Ali, M.A. Rahman, Micro-electro discharge machining of non-conductive zirconia ceramic: investigation of MRR and recast layer hardness, Int. J. Adv. Manuf. Technol. 75 (2014) 257–267.

[105] A. Muttamara, Y. Fukuzawa, N. Mohri, T. Tani, Effect of electrode material on electrical discharge machining of alumina, J. Mater. Process. Technol. 209 (2009) 2545–2552.

[106] K. Liu, J. Peirs, E. Ferraris, B. Lauwers, D. Reynaerts, Micro Electrical Discharge Machining of Si_3N_4 -based Ceramic Composites, Energy Convers. (2008).

[107] Y. Fukuzawa, N. Mohri, T. Tani, A. Muttamara, Electrical discharge machining properties of noble crystals, J. Mater. Process. Technol. 149 (2004) 393–397.

[108] B. Lauwers, J.P. Kruth, W. Liu, W. Eeraerts, B. Schacht, P. Bleys, Investigation of material removal mechanisms in EDM of composite ceramic materials, J. Mater. Process. Technol. 149 (2004) 347–352.

[109] K. Bonny, P. De Baets, J. Vleugels, A. Salehi, O. Van der Biest, B. Lauwers, W. Liu, Influence of secondary electro-conductive phases on the electrical discharge machinability and frictional behaviour of ZrO_2-based ceramic composites, J. Mater. Process. Technol. 208 (2008) 423–430.

[110] S. Salehi, O. Van der Biest, J. Vleugels, Electrically conductive ZrO_2–TiN composites, J. Eur. Ceram. Soc. 26 (2006) 3173–3179.

[111] K. Bonny, P. De Baets, J. Vleugels, O. Van der Biest, A. Salehi, W. Liu, B. Lauwers, Reciprocating sliding friction and wear behaviour of electrical discharge machined zirconia-based composites against WC–Co cemented carbide, Int. J. Refract. Met. Hard. Mater. 27 (2009) 449–457.

[112] T.H. Hocheng, Machining Technology for Composite Materials. Principles and Practice, Elsevier Science, 2011.

[113] K. Bonny, P. De Baets, J. Vleugels, A. Salehi, O. Van Der Biest, B. Lauwers, W. Lieu, EDM machinability and frictional behaviour of ZrO_2-WC composites, Int. J. Adv. Manuf. Technol. 41 (2009) 1085–1093.

[114] B. Lauwers, K. Brans, W. Liu, J. Vleugels, S. Salehi, K. Vanmeensel, Influence of the type and grain size of the electro-conductive phase on the Wire-EDM performance of ZrO_2 ceramic composites, CIRP Ann. Manuf. Technol. 57 (2008) 191–194.

[115] A. Balandin, Thermal properties of graphene and nanostructured carbon materials, Nat. Mater. 10 (2011) 569–581.

[116] S.R. Bakshi, K. Balani, A. Agarwal, Thermal Conductivity of Plasma-Sprayed Aluminum Oxide—Multiwalled Carbon Nanotube Composites, J. Am. Ceram. Soc. 91 (2008) 942–947.

[117] L. Kumari, T. Zhang, G. Du, W. Li, Q.W. Wang, A. Datye. K.H. Wu, Thermal properties of CNT-Alumina nanocomposites, Compos. Sci. Technol. 68 (2008) 2178–2183.

[118] H.L. Zhang, J.F. Li, K.F. Yao, L.D. Chen, Spark plasma sintering and thermal conductivity of carbon nanotube bulk materials, J. Appl. Phys. 97 (2005) 10–15.

[119] Q. Huang, L. Gao, Multiwalled carbon nanotube/BaTiO nanocomposites: Electrical and rectification properties, Appl. Phys. Lett. 86 (2005) 123104.

[120] R. Sivakumar, S. Guo, T. Nishimura, Y. Kagawa, Thermal conductivity in multi-wall carbon nanotube/silica-based nanocomposites, Scr. Mater. 56 (2007) 265–268.

[121] L. Jiang, L. Gao, Densified multiwalled carbon nanotubes-titanium nitride composites with enhanced thermal properties, Ceram. Int. 34 (2008) 231–235.

[122] http://www.tosoh.com/our-products/advanced-materials/zirconia-powders

[123] C. Laurent, E. Flahaut, A. Peigney, The weight and density of carbon nanotubes versus the number of walls and diameter, Carbon N. Y. 48 (2010) 2994–2996.

[124] L.A. Giannuzzi, F.A. Stevie, A review of focused ion beam milling techniques for TEM specimen preparation, Micron. 30 (1999) 197–204.

[125] H. Toraya, M. Yoshimura, S. Somiya, Calibration Curve for Quantitative Analysis of the Monoclinic-Tetragonal ZrO_2 System by X-Ray Diffraction, Commun. Am. Ceram. Soc. (1984) 119–121.

[126] D. Munz, T. Fett, Ceramics: Mechanical Properties, Failure Behaviour, Materials Selection, Springer, 1999.

[127] W.C. Oliver, G.M. Pharr, Measurement of hardness and elastic modulus by instrumented indentation: Advances in understanding and refinements to methodology, J. Mater. Res. 19 (2011) 3–20.

[128] A. Tiwari, Nanomechanical Analysis of high performance materials, 2013.

[129]http://www.adhesivestoolkit.com/Docs/test/MECHANICAL%20TEST%2 METHOD%201%20-%20Continued.xtp /

[130] ASTM Standard E2585-09, ASTM Standard E2585-09: Standard Practice for Thermal Diffusivity by the Flash Method, ASTM Int. (2009).

Part II

Summary of Papers

Paper I
Coefficient of friction and wear resistance of zirconia-MWCNTs composites.

Summary: The wear rate of 3Y-TZP /3Y-TZP is high in comparison to other ceramic pairs like alumina/alumina because of the surface fracture induced by microcracking during phase transformation. Moreover, the low thermal conductivity of zirconia induces a substantial increase in temperature in the contact zone and weakens the material. Therefore, the incorporation of relatively low weight fraction of CNTs in zirconia matrix can reduce the wear rate and lower the friction coefficient.

In the present paper, the friction coefficient and the wear rate of SPS zirconia-MWCNT composites were determined. The addition of MWCNT from 0.5 to 2 wt % resulted in reduction of 3Y-TZP grain size from 174 to 148 nm respectively. The effect of the addition of MWCNT on the coefficient of friction (COF) was studied. Nano-scratch and macro-scratch tests were conducted using diamond Berkovich and Rockwell indenter, respectively. Furthermore, the wear rate was also investigated using reciprocating sliding under a load of 5 N. It was found that the COF decreased with the increase in MWCNT content. However, in macro-scratch testing, there was a critical load over which brittle fracture sets in and its value decreases as the MWCNT content increases. The wear resistance was found to be decreasing very slightly for MWCNT content less than 1 wt %. However, wear resistance increases strongly for the addition of 2 wt % MWCNT.

Author contributions: The powder processing of the composites and all the experiments were performed by the author, except for the nanoindentation test which

was performed by co-author Joan Josep Rovira. Data evaluation and discussion were drawn by the author together with Prof. Marc Anglada. Writing of this article was accomplished by the author.

Paper II
Nanoindentation and fracture toughness of nanostructured zirconia/multi-walled carbon nanotube composites.

Summary: The fracture toughness (K_{Ic}) in 3Y-TZP can be increased by promoting phase transformation from tetragonal (*t*) to monoclinic (*m*) phase in front of a propagating crack tip referred to transformation toughening. However, the stronger the tendency for stress induced transformation, the higher the risk for premature spontaneous *t-m* transformation in humid atmosphere. This is called hydrothermal degradation or low temperature degradation (LTD) and can result in microcracking and loss of strength. This phenomenon is the main drawback for the wider use of 3Y-TZP. The resistance to LTD can be increased by reducing the grain size into the nanoscale by using Spark Plasma Sintering (SPS). However, the reduction of grain size will reduce the transformation toughening and the fracture toughness will decrease.

In the current study MWCNTs have been used as a toughening phase due to their excellent mechanical properties. On the other hand, the "true" K_{Ic} of the composites is still under debate since the indentation method is not an accurate method as it overestimates the values of K_{Ic}.

In the current study, a novel and accurate method for the calculation of "true" K_{Ic} was developed. The method is based on producing a very sharp notch with submicrometer radius less than 0.5 μm using Ultra-short Pulsed Laser Ablation (UPLA). It was found that "true" K_{Ic} of the composites with CNT content ranging from 0.5 up to 2 wt % CNT is hardly increasing with the addition of CNTs content while the indentation fracture toughness is increasing. Hence, the resistance to indentation cracking of the composites by adding CNTs to 3Y-TZP matrix does not indicate higher true fracture toughness. The reasons of the low K_{Ic} of the composites could be related to the drop in hardness and elastic modulus found using Berkovich nanoindentation.

Author contributions: The preparation of the composite powders was accomplished by the author. Mechanical testing and damage analysis were accomplished by the author. The nanoindentation test was performed by co-author Joan Josep Rovira. The discussion and the analysis of the results were drawn together by the author and Prof. Marc Anglada.

Paper III
The influence of unshielded small cracks in the fracture toughness of yttria and of ceria stabilised zirconia used in medical applications.

Summary: Based on fracture mechanics criteria, if the critical natural flaw and the fracture toughness are precisely determined, then it is possible to predict the strength of advanced ceramics.
In the present work, the novel method Ultra-short Pulsed Laser Ablation (UPLA) was used to investigate the influence of transformation toughening on the strength and on the fracture toughness of both 12Ce-ZrO_2 and 3Y-TZP with two different grain sizes; 300 nm and 177 nm. A sharp notch induced using UPLA in 300 nm-3Y-TZP, 177 nm-3Y-TZP and 12Ce-ZrO_2 results in similar and small cracks in both materials. Three regions can be distinguished from the fracture surface of the samples; the region of the notch (zone A), the micro-crack region (zone B) and the final fracture (zone C). The notch plus micro-cracked region act as unshielded sharp crack and the effective fracture toughness was found to be similar for all studied materials in spite of the large differences in plateau and steepness of their R-curves.
The strength of 330 nm-3Y-ZrO_2 is much higher compared to the strength of 12Ce-ZrO_2 which has higher grain size and higher transformation induced fracture in specimens with natural cracks. However, by inducing a very sharp notch using UPLA, the initial crack size from which fracture takes place is practically the same in both materials and the difference in strength is only about 10 %. Therefore, the beneficial effect of higher indentation fracture toughness in 12Ce-ZrO_2 in comparison with 3Y-ZrO_2, widely referred in the literature, has a very small effect on the real effective fracture toughness that determines the strength of unshielded small cracks.

Author contributions: The preparation of the specimens was accomplished by the author and co-author Miquel Turron-Vinas. The processing of the laser notch using UPLA method was manufactured by Dr. Pablo Moreno Pedraz at the University of Salamanca. Mechanical testing and all characterization techniques were carried out by the author. The discussion and the writing were accomplished by the author and Prof. Marc Anglada.

Paper IV
Material removal mechanisms by EDM of zirconia reinforced MWCNT nanocomposites.

Summary: Zirconia ceramic has good mechanical properties and therefore a wide range of applications. However, its high hardness and brittleness limits its ability to be machined with conventional techniques. Electrical Discharge Machining (EDM) is one of the most promising techniques to machine ceramic matrix composites. Nevertheless, a crucial requirement in the use of EDM is the need for an electrically conductive work piece.
In the current paper, the effect of MWCNT on the electrical conductivity and the machinability of the composites were studied. Moreover, the thermal conductivity of the composites at two different SPS temperatures; 1350 °C and 1500 °C, was investigated. The damage produced and the material removal mechanisms were investigated after EDM machining.
It was found that the studied zirconia-MWCNT composites have high electrical conductivity which results in successful EDM machining of the composites with 1 and 2 wt % CNT content. However, there was only a relatively small increase of thermal conductivity with the addition of MWCNTs. A recast layer was found on the surface after machining where zirconium carbide (ZrC) was detected. The material removal mechanisms were found to be melting/evaporation and spalling.

Author contributions: The composites powder processing was done by the author. Damage characterization after EDM was done by the author. Electrical and thermal conductivities were measured by the author with the help of co-authors Andreas Kaiser and Nikolaos Bonanos at Technical University of Denmark (DTU). EDM was performed by the company Zentrum für Mechatronik und Automatisierungstechnik (ZeMA) in Germany. The writing of the paper was accomplished by the author.

Paper V
Surface microstructural changes of Spark Plasma Sintered zirconia after grinding and annealing

Summary: Machining zirconia ceramics is considered as a crucial step in the manufacturing of long lasting and strong zirconia components. The damage induced by machining zirconia ceramics could affects it´s integrity and reliability.
In the present study, an investigation of the effect of grinding was conducted on 3Y-TZP sintered using SPS at different temperatures; 1350 °C, 1450 °C and 1600 °C. A

thermal etching at 1100 °C for one hour of the ground samples revealed the presence of a nano-grain layer of about 60 μm grain sizes independent of the SPS temperature. The thickness of the nano-grain layer was in the order of few hundred nanometers. This nanograin layer is formed by recrystallization of a very thin highly deformed surface layer produced during grinding. Moreover, a heat treatment in air at 1200 °C of the ground samples showed that the surface grain size increases fast but it still remains smaller than in the starting polished specimens. Finally, when the ground layer is exposed to 1575 °C annealing temperature, the surface grains grow to a size which is roughly similar to that achieved in polished specimens by heat treatment to the same temperature. The formation of the nano-grain layer could increase the resistance to LTD of zirconia ceramics. Furthermore, it may be of interest when a rough surface is beneficial as for example for implants since roughness favours osseointegration.

Author contributions: The powder processing of the composites was done by the author. The SPS of samples was conducted by co-author Farid Akhtar. The experiments were performed by the author. The SEM image analysis was carried out together by the author and co-author Johanne Mouzon. The writing of the paper was completed by the author. All the co-authors participated in the improvements of the paper.

Part III

Paper I

Coefficient of friction and wear resistance of zirconia–MWCNTs composites

Authors:
Latifa Melk, Joan Josep Roa, Marta-Lena Antti and Marc Anglada

Paper Published in:
Journal of Ceramics International, 41 (2014) 459-468.

ATTENTION ¡
Pages 70 to 80 of the thesis are available at the editor's web
http://www.sciencedirect.com/science/article/pii/S0272884214013297

Paper II

Nanoindentation and fracture toughness of nanostructured zirconia/multi-walled carbon nanotube composites

Authors:
Latifa Melk, Joan Josep Roa, Fernando García-Marro, Marta-Lena Antti, Ben Milsom, Mike J. Reece and Marc Anglada.

Paper Published in:
Journal of Ceramics International, 41 (2015) 2453-2461.

ATTENTION ¡
Pages 82 to 92 of the thesis are available at the editor's web
http://www.sciencedirect.com/science/article/pii/S0272884214015855

Paper III

The influence of unshielded small cracks in the fracture toughness of yttria and of ceria stabilised zirconia

Authors:
Latifa Melk, Miquel Turón-Viñas, Joan Josep Roa, Marta-Lena Antti and Marc Anglada.

Paper Published in:
Journal of the European Ceramic Society, 36 (2016) 147–153.

ATTENTION ¡
Pages 94 to 102 of the thesis are available at the editor's web
http://www.sciencedirect.com/science/article/pii/S0955221915301369

Paper IV

Material removal mechanisms by EDM of zirconia reinforced MWCNT nanocomposites

Authors:
Latifa Melk, Marta-Lena Antti and Marc Anglada.

Paper Published in:
Journal of Ceramic International, 42 (2016) 5792-5801.

ATTENTION ¡
Pages 104 to 114 of the thesis are available at the editor's web
http://www.sciencedirect.com/science/article/pii/S0272884215024189

Paper V

Surface microstructural changes of Spark Plasma Sintered zirconia after grinding and annealing

Authors:
Latifa Melk, Johanne Mouzon, Farid Akhtar, Miquel Turón-Viñas, Marta-Lena Antti and Marc Anglada.

To be submitted

Surface microstructural changes of Spark Plasma Sintered zirconia after grinding and annealing

Latifa Melk [a, b, c, e], Johanne Mouzon[d], Miquel Turon[a,b], Farid Akhtar[c], Marta-Lena Antti[c], Marc Anglada[a,b]

[a] CIEFMA-Department of Materials Science and Metallurgical Engineering, ETSEIB, Universitat Politècnica de Catalunya, 08028 Barcelona, Spain

[b] CRnE, Campus Diagonal Sud, Edifici C', Universitat Politècnica de Catalunya, 08028 Barcelona, Spain

[c] Department of Engineering Sciences and Mathematics, Luleå University of Technology, 97187 Luleå, Sweden

[d] Department of Civil, Environmental and Natural Resources Engineering, Luleå University of Technology, 97187 Luleå, Sweden

[e] Corresponding author at: Department of Materials Science and Engineering/ETSEIB
Diagonal 647. 08028-Barcelona
Tel. +34 934016701
Fax. +34 934016706
E-mail: melk.latifa@gmail.com

Abstract

Spark plasma sintered zirconia (3Y-TZP) specimens have been produced of 140 nm 372 nm and 753 nm grain sizes by sintering at 1250 °C, 1450 °C and 1600 °C, respectively. The sintered zirconia specimens were grinded using a diamond grinding disc with an average diamond particle size of about 60 μm, under a pressure of 0.9 MPa. The influence of grinding and annealing on the grain size has been analysed. It was shown that thermal etching after a ruff grinding of specimens at 1100 °C for one hour induced an irregular surface layer of about a few hundred nanometres in thickness of recrystallized nano-grains, independently of the initial grain size. However, if the ground specimens were exposed to higher temperature, e.g. annealing at 1575 °C for one hour, the nano-grain layer was not observed and the final grain size was similar to that achieved by the same heat treatments on carefully polished specimens. Therefore, by appropriate grinding and thermal etching treatments, nanograined surface layer can be obtained which increases the resistance to low temperature degradation.

Keywords: zirconia, grinding, annealing, low temperature degradation

1 Introduction

Yttria stabilised tetragonal polycrystalline zirconia (3Y-TZP) has a wide range of applications, especially in the medical sector, because of its biocompatibility and very good mechanical properties, such as strength and toughness. The local and constrained phase transformation from tetragonal (*t*) to monoclinic (*m*) structure generates compressive stresses at the crack tip which enhances toughness. However, 3Y-TZP suffers from surface spontaneous *t-m* transformation in humid atmosphere, often referred to as hydrothermal degradation, aging or low temperature degradation (LTD), which is accompanied by formation of near surface microcracks and loss of surface mechanical properties [1–4].

During the processes of final shaping and surface finishing, 3Y-TZP may be subjected to different machining processes (cutting, polishing, grinding, and milling). The damage induced by machining affects structural integrity and reliability of the material. Therefore, machining zirconia is considered as a critical step in the manufacturing of long lasting and strong 3Y-TZP components.

Previous investigations have shown that grinding influences the surface integrity and the flexural strength of 3Y-TZP materials [5]. Therefore, most of the studies on ground zirconia have focussed on characterizing surface microstructural changes that may affect the chemical and mechanical behaviour. The main changes frequently observed in the X-ray diffraction (XRD) spectrum are the following: (1) *t–m* phase transformation; (2) asymmetrical broadening of the (1 1 1) tetragonal peak at ~30° (2θ); (3) intensity reversal of the tetragonal doublet at 34.64° and 35.22° (2θ) corresponding to the (0 0 2) and (2 0 0) planes [6–10]. On the other hand, a TEM investigation of the ground surface by Munoz et al. [11] reported the existence of three different regions from the ground surface towards the bulk : (1) a recrystallized zone, exactly at the surface, where the grains have a diameter in the range 10–20 nm; (2) a plastically deformed zone; (3) a *t-m* transformed zone, which is mainly responsible for the formation of compressive residual stresses that usually increase the flexure strength and the apparent fracture toughness of ground specimens [11].

The near surface monoclinic phase formed during machining operations can be reversed to tetragonal by annealing. The operation of grinding and the time and temperature of annealing have an influence on the resistance to LTD, which can be inhibited or delayed [12]. The evolution of the resistance to LTD of specimens of initially 330 nm grain size subjected to grinding and annealing at 1200 °C for different times (1 min, 10 min and 1h) was analysed by Muñoz et al.

[13]. The results showed that LTD of ground 3Y-TZP was supressed due to the formation of a recrystallized nano-grain layer on the surface. Moreover, the resistance to LTD was decreasing during long time annealing at 1200 °C after that grain size reached grew beyond the initial surface grain size of 330 nm. The effect of different high annealing temperatures in the range 1200 °C - 1600 °C on the surface microstructure of ground zirconia was recently studied by Roa et al. [14]; this group also found the recrystallized surface nano-grain layer after annealing at 1200 °C by milling a small cross section of the near surface region by FIB/SEM, while at 1600 °C the near surface microstructure was composed of larger grain sizes than the grain size of the bulk material.

To the best of our knowledge, previous studies of the effect of grinding on 3Y-TZP have been carried out only on conventionally sintered zirconia with grain size in the range of approximately 330 nm. The present work is focussed on the analysis of surface microstructural changes after grinding and annealing Spark Plasma Sintered (SPS) zirconia with different initial grain sizes of 140 nm, 370 nm and 750 nm achieved by sintering at 1250 °C, 1450 °C and 1600 °C, respectively.

2 Experimental

2.1 Material processing

Zirconia powder stabilized with 3 mol % of yttria (TZ-3YSB-E, Tosoh, Tokyo, Japan) with a crystalline size of 36 nm was sintered using spark plasma sintering (SPS) at 1250 °C, 1450 °C and 1600 °C for 5 minutes. The pressure maintained during the sintering cycle was 55 MPa and the heating rate was 100 °C/min.

The final samples were ceramic discs (50 mm x 3 mm). The average grain size was determined using the line intercept method on SEM images and the density was measured by the Archimedes method**.**

The samples were ground using a new diamond grinding disc (MD-Piano 220 Struers) with an average particle size of about 60 μm, under a pressure of 0.9 MPa with a constant grinding speed of 3.6 m/s in one direction and water cooling. The selection of this grinding condition was based on a previous work of Juy et al. [15], who found that these particular parameters produce an increase in mechanical properties. The samples were then thermally etched at 1100 °C for 1 hour in standard furnace in air in order to observe grain size in the scanning electron microscope (SEM).

The samples studied will be referred to as SPS 1250, SPS 1450 and SPS 1600 according to the temperature used for sintering at 1250 °C, 1450 °C and 1600 °C, respectively. The samples were divided into two batches. The first batch corresponds to the as-ground samples which are referred in the current study as ASgr (AS ground). In order to reveal the grain size of the ASgr samples, they were maintained at 1100 °C for 1 hour for thermal etching, 1200 °C for annealing, and at 1575 °C for high temperature annealing. The second batch consists of specimens that were polished starting with 9 μm diamond down to 1 μm and finally polished with colloidal silica. The polished samples were subjected to the same heat treatment temperatures, and are herein referred to as ASpol (AS polished). In fact, each heat treatment on ground and polished specimens was carried out on the very same sample by polishing one face of the disc and grinding the other face in order to ensure that both faces were exactly subjected to the same temperature during annealing.

2.2 Mechanical testing

Hardness was measured by Vickers indentation with a load of 98.1 N. The cracks emanating from the vertex of the residual impressions were used to measure indentation fracture toughness using Niihara equation [16] taking into account the observed Palmqvist configuration of the indentation cracks. Anstis et al. [17] equation was also applied for comparative purposes. However, as extensively reported in the literature [18], indentation fracture toughness does not really represent the "true" fracture toughness (K_{Ic}) of the material. Therefore, the fracture toughness measurements in the present work have been used only as an indication of *t-m* transformability under localised sharp contact of compressive loads.

2.3 Surface Analysis

The crystallographic phases were identified by X-ray diffraction (XRD) with Bragg-Brentano symmetric-geometry, using PANalytical Empyrean equipment with PIXcel-3D detector and Cu-Kα (45kV and 40mA) radiation. The XRD spectra were obtained in a scan range of $20° \leq 2\theta \leq 100°$, using a step size of 0.013° and an anti-scatter slit of 1°. The monoclinic phase content was calculated by the equation proposed by Toraya et al. [19].

$$V_m = \frac{1.311 \times (I_m^{(\bar{1}11)} + I_m^{(111)})}{1.311 \times \left(I_m^{(\bar{1}11)} + I_m^{(111)}\right) + I_t^{(111)}}$$

Surface damage analysis of all the specimens was performed by extreme high resolution scanning electron microscopy (XHR-SEM) (Magellan 400, FEI Company) at an acceleration voltage of 3 kV. Microstructural changes below the surface induced during the grinding process were investigated by preparing thin cross-sections using focused ion beam (FIB). Cross sectioning observations were conducted using a dual beam workstation (Zeiss Neon 40). A thin platinum layer was deposited on the sample prior to FIB with the aim of reducing ion-beam damage. A Ga+ ion source was used to mill the surface at a voltage of 30 kV. Final polishing of the cross-section was performed at a current of 500 pA.

3 Results and discussion

The present study shows clearly that the use of SPS results in dense zirconia samples of about 99 % of theoretical density, see **Table 1**. SPS is a highly efficient technique for the densification of zirconia ceramics compared with conventional sintering such as Hot Pressing (HP) for example. Self-heating from spark discharge between the particles could be the reason behind the low temperature and short time for sintering. It has been found that during SPS the residual gases in the powder will be efficiently removed as long as the system is open. As the pressure will not be applied until the isothermal temperature is reached, CO_2(g) and H_2O(g) can then escape before the densification starts [20].

Furthermore, by increasing the SPS temperature, the grain size increases from 140 nm to 750 nm for SPS 1250 and SPS 1600, respectively, see **Table 2** and **Fig. 1**. It has been reported that the presence of an electric field could enhance the grain growth in yttria-stabilized cubic zirconia by increasing the grain boundary mobility [21]. Moreover, a dependency was shown between grain size and the heating-rate which promoted grain growth by increasing the defect concentration [22].

Fig. 2 shows the XRD spectra of ASgr in all SPS zirconia samples. It can be observed the presence of a broadening of the tetragonal peaks and that the tetragonal peak at $2\theta \approx 30°$ that corresponds to $(111)_t$ has a speak shoulder that may correspond to either the rhombohedral phase or to distorted tetragonal phase as was reported in [14]. The presence of monoclinic phase at $2\theta \approx 28°$ and 16° was also observed. It has been found that the monoclinic phase detected in ASgr is 13 %, 14 % and 12 % for SPS 1250, SPS 1450 and SPS 1600 respectively, see **Fig. 3**.

After annealing at 1200 °C and 1575 °C, the peak shoulder disappears and no monoclinic phase is detected due to the *m-t* transformation that actually starts at lower temperatures [23]. It could also be observed that the intensity of (002) and (200) tetragonal peaks at 2θ=34°, 64° and 35,22° is reversed compared to the ASpol. In ASpol, the intensity ratio of $I_t^{(002)}/I_t^{(200)}$ is equal to 0.45 while in ASgr annealed at 1575 °C, $I_t^{(002)}/I_t^{(200)}$ the ratio is equal to 1.63. This is attributed to the texture due stress induced reorientation from ferroelastic domain switching [7].

Indentation fracture toughness is similar to that for conventionally sintered 3Y-TZP with similar grain size, independently of the indentation equation used for calculating the fracture toughness. On the other hand, there is a small decrease in hardness with grain size which may be related to a higher transformability as the grain size increases, see **Table 2**.

The specimens ASgr with subsequent thermal etching at 1100 °C for 1 hour show a nanometric grain size on the surface as can be seen on the images of left column of **Fig. 3**. The larger grain size observed in ASgr was always much smaller than the average grain size in ASpol. After thermal etching at 1100 °C, the grain size in the ASgr was reduced by a factor of 2 compared to the ASpol in SPS 1250 and by a factor of 10 in SPS 1575. However, if ASgr specimens are annealed at 1200 °C or 1545 °C, the surface grain size increases fast and it reaches dimensions roughly similar to as ASpol specimens subjected to the same high temperature treatment. This can be appreciated by comparing ASgr and ASpol specimens under the same heat treatment (see **Fig. 3**).

The analysis of sections perpendicular to the surface obtained by FIB (**Fig. 4**) shows that there is a very thin layer of surface damage on ASgr specimens after grinding. The layer extends to depths of only a few hundred nanometers. The depth is not uniform and it changes from one place to another. It is deeper close to places where the material is piling up at the side of the grinding scratches. The same observation was carried out after annealing and they are shown in **Fig. 5**.

Fig. 5 shows the presence of the nano-grain layer with a depth corresponding to the same depth of the nano-grain layer seen in the ground specimens before annealing.

The existence of this surface nano-grain size layer on thermal etched ASgr specimens can also be detected on the fracture surface of specimens as shown in **Fig. 6** where the fracture surface of ASpol and ASgr are compared. The presence of nano-grain layer in the etched ASgr specimens can be clearly observed. This

nano-grain layer is formed by recrystallization of a very thin highly deformed surface layer produced during grinding. Since the usual procedure to observe the grain size is by means of grinding with decreasing diamond particle size and careful polishing, the damage layer is finally removed so that no recrystallization is detected during standard specimen preparation and thermal etching for grain size determination.

In one the earliest investigations on this topic, it was shown that this recrystallized nanometric layer can be useful for preventing hydrothermal degradation because the resistance to LTD increases as the zirconia grain size decreases [12]. The requirement of a smooth polished surface for many applications makes this procedure feasible when a specular smooth surface finish is not required. It may be of interest when a rough surface is beneficial as for example for implants since roughness favours osseointegration [24].

Regarding the influence of the surface damage induced by grinding on the strength, it was shown that it does not affect the strength of ground specimens. On the contrary, grinding induces the formation of a compressive surface layer which results in an increase of the strength [25,26]. However, after thermal etching and recrystallization, the compressive forces disappear as monoclinic phase is transformed back to tetragonal and then the strength may slightly decrease depending on the damage induced by grinding [11].

It is still unknown how much minimum plastic deformation by grinding is needed in order to form nanocrystals during etching. It will be interesting to find out which are the weakest grinding conditions for which recrystallization still takes place during thermal etching. **Fig. 7** shows a shallow scratch left on a polished surface where recrystallization still takes place in and around the scratch. This shows that the recrystallization could still remain after polishing if a deep scratch is not fully removed by subsequent operations of grinding with smaller particle size followed by polishing.

4 Conclusions

Spark plasma sintered 3Y_TZP specimens have been produced with different grain sizes of 140 nm, 372 nm and 753 nm by sintering at 1250 °C, 1450 °C and 1600 °C. The influence of grinding and annealing has been analysed. Two main conclusions can be derived from the present work: a) the effect of the grinding conditions used in this study induces a few hundred nanometer surface layer which recrystallizes during thermal etching at 1100 °C. The surface layer

contains recrystallized nano-grains with a grain size smaller and practically independent of the initial grain size depending on the SPS temperature. This behaviour is similar to that of conventionally sintered zirconia specimens; b) if the ground layer is exposed to higher annealing temperatures, the nano-grain layer disappears and the surface grains grow to a size which is similar to that achieved in polished specimens by heat treatment to the same temperature.

Acknowledgements

The authors gratefully acknowledge the financial support given by the "Ministerio de Ciencia e Innovación", Spain through research grant MAT2011-23913. The authors acknowledge the EU for financial support through the e-Create-Network of the Rise program. L. Melk acknowledges the fellowship award received from the European Joint Doctoral Programme in Materials Science and Engineering (DocMASE) of the European Union. Finally, all authors thank Dr. Trifon Trifonov and Dr. Joan Josep Roa from UPC for their assistance in the FIB/SEM equipment.

References

[1] K. Kobayashi, H. Kuwajima, T. Masaki, Phase change and mechanical properties of ZrO_2-Y_2O_3 solid electrolyte after ageing, Solid State Ionics. 3 1981)489–493.

[2] M. Yoshimura, T. Noma, K. Kawabata, S. Somiya, Role of H_2O on the degradation process of Y-TZP, J. Mat. Sci Lett. 6 (2000) 465–467.

[3] S. Lawson, Environmental Degradation of Zirconia Ceramics, J. Eur. Ceram. Sci. 15 (1995) 485–502.

[4] J. Chevalier, L. Gremillard, A. V. Virkar, D.R. Clarke, The Tetragonal-Monoclinic Transformation in Zirconia: Lessons Learned and Future Trends, J. Am. Ceram. Soc. 92 (2009) 1901–1920.

[5] T. Kosmač, Č. Oblak, P. Jevnikar, N. Funduk, L. Marion, Strength and reliability of surface treated Y-TZP dental ceramics, J. Biomed. Mater. Res. 53 (2000) 304–313.

[6] H. Hasegawa, Rhombohedral phase produced in abraded surfaces of partially stabilized zirconia (PSZ), J. Mater. Sci. Lett. 2 (1983) 91–93.

[7] A. V. Virkar, R.L.K. Matsumoto, Ferroelastic Domain Switching as a Toughening Mechanism in Tetragonal Zirconia, J. Am. Ceram. Soc. 69 (1986) C–224–C–226.

[8] J. Kitano, Y. Mori, A. Ishitani, T. Masaki, A Study of Rhombohedral Phase in Y_2 O_3 -Partially Stabilized Zirconia, MRS Proc. 78 (1986) 17.

[9] N. Mitra, K. Vijayan, B. Bai, S.K. Biswas, Phase Transformation Introduced by Mechanical and Chemical Surface Preparations of Tetragonal Zirconia Polycrystals, J. Am. Ceram. Soc. 76 (1993) 533–535.

[10] D.P. Burke, W.M. Rainforth, Intermediate rhombohedral (r-ZrO_2) phase formation at the surface of sintered Y-TZP's, J. Mater. Sci. Lett. 16 (1997) 883–885.

[11] J.A. Munz-Tabares, E. Jiménez-Piqué, J. Reyes-Gasga, M. Anglada, Microstructural changes in ground 3Y-TZP and their effect on mechanical properties, Acta Mater. 59 (2011) 6670–6683.

[12] P.J. Whalen, F. Reidinger, R.F. Antrim, Prevention of low-temperature surface transformation by surface recrystallization in yttria-doped tetragonal zirconia, J. Am. Ceram. Soc. 72 (1989) 319–321.

[13] J.A. Muñoz-Tabares, M. Anglada, Hydrothermal degradation of ground 3Y-TZP, J. Eur. Ceram. Soc. 32 (2012) 325–333.

[14] J.J. Roa, M. Turon-Vinas, M. Anglada, Surface grain size and texture after annealing ground zirconia, J. Eur. Ceram. Soc. 36 (2016) 1519–1525.

[15] A. Juy, M. Anglada, Surface phase transformation during grinding of Y-TZP, J. Am. Ceram. Soc. 90 (2007) 2618–2621.

[16] K. Niihara, A fracture mechanics analysis of indentation-induced Palmqvist crack in ceramics, J. Mater. Sci. Lett. 2 (1983) 221–223.

[17] G.R. Anstis, P. Chantikul, B.R. Lawn, D.B. Marshal, A critical evaluation of indentation techniques for measuring fracture toughness: I Direct crack measurements, J. Am. Ceram. Soc. 46 (1981) 533–538.

[18] G.D. Quinn, R.C. Bradt, On the Vickers Indentation Fracture Toughness Test, J. Am. Ceram. Soc. 90 (2007) 673–680.

[19] H. Toraya, M. Yoshimura, S. Somiya, Calibration Curve for Quantitative Analysis of the Monoclinic-Tetragonal ZrO_2 System by X-Ray Diffraction, Commun. Am. Ceram. Soc. (1984) 119–121.

[20] P. Dahl, I. Kaus, Z. Zhao, M. Johnsson, M. Nygren, K. Wiik, et al., Densification and properties of zirconia prepared by three different sintering techniques, Ceram. Int. 33 (2007) 1603–1610.

[21] S.W. Kim, S.G. Kim, J. Il Jung, S.J.L. Kang, I.W. Chen, Enhanced grain boundary mobility in yttria-stabilized cubic zirconia under an electric current, J. Am. Ceram. Soc. 94 (2011) 4231–4238.

[22] B.N. Kim, K. Hiraga, K. Morita, H. Yoshida, Effects of heating rate on microstructure and transparency of spark-plasma-sintered alumina, J. Eur. Ceram. Soc. 29 (2009) 323–327.

[23] O. Fabrichnaya, F. Aldinger, Assessment of thermodynamic parameters in the system ZrO_2-Y_2O_3-Al_2O_3, Zeitschrift Für Met. 95 (2004) 27–39.

[24] Q. Flamant, F. García Marro, J.J. Roa Rovira, M. Anglada, Hydrofluoric acid etching of dental zirconia. Part 1: etching mechanism and surface characterization, J. Eur. Ceram. Soc. 36 (2016) 121–134.

[25] A. Juy, L. Llanes, M. Anglada, Strength of Yttria-Stabilised Zirconia with Near-Surface Grinding Residual Stresses, ECF14, Cracow 2002. (2013).

[26] T. K. Gupta, Strengthening by Surface Damage in Metastable Tetragonal Zirconia, J. Am. Ceram. Sci. 63 (1980) 117.

Tables

Table 1. *Density and grain size of the SPS zirconia specimens before and after annealing.*

		Temperature/Grain size					
Specimen	Density ($g.cm^{-3}$)	1100°C ASpol (nm)	1100°C ASgr (nm)	1200°C ASpol (nm)	1200°C ASgr (nm)	1575°C ASpol (nm)	1575°C ASgr (nm)
SPS1250	6.00 ±0.03	140±10	59±7	144±16	105±9	611±93	602±153
SPS1450	5.99± 0.09	372±50	66±15	386±29	149±22	699 ±79	896±167
SPS1600	6.05± 0.04	753±60	67±11	658±76	±	856±57	708±97

Table 2. *Vickers hardness and indentation fracture toughness of the SPS zirconia samples.*

Specimen	Vickers hardness (HV10) (GPa)	Indentation K_{IC} (Niihara) (MPa·m1/2)	Indentation K_{IC} (Anstis) (MPa·m1/2)
SPS 1250	14.7±0.2	5.2±0.1	3.9±0.2
SPS 1450	13.8±0.1	5.1±0.1	3.8±0.1
SPS 1600	13.6±0.2	5.2±0.1	4.0±0.1

Figures

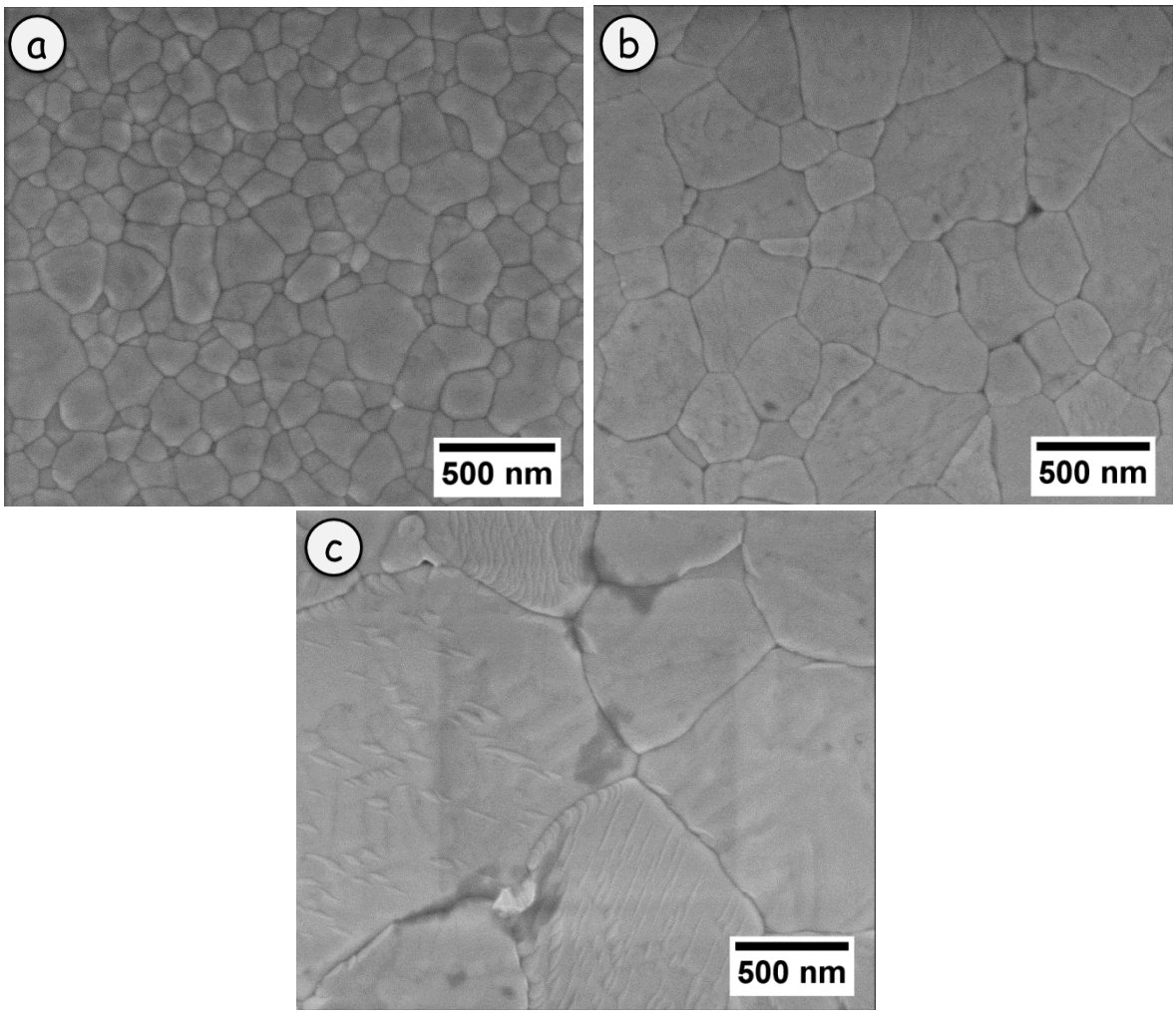

Fig. 1 *SEM images showing the microstructure of ASpol after thermal etching at 1100 °C for 1h:* ***a)*** *SPS 1250* ***b)*** *SPS1450 and* ***c)*** *SPS1600.*

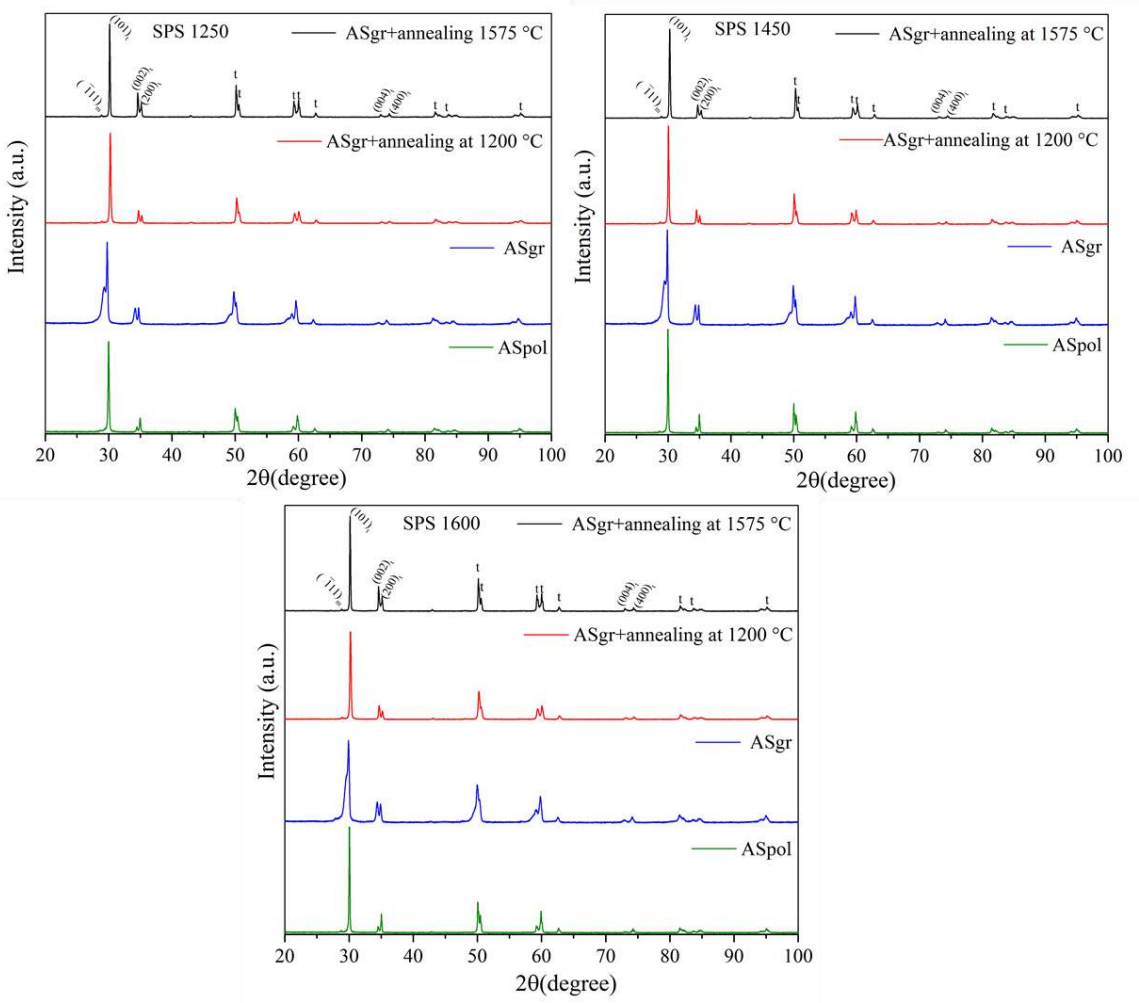

Fig. 2 *XRD spectra of SPS zirconia ASpol, ASgr, ASgr+annealed at 1200 °C and ASgr+annealed at 1575 °C.*

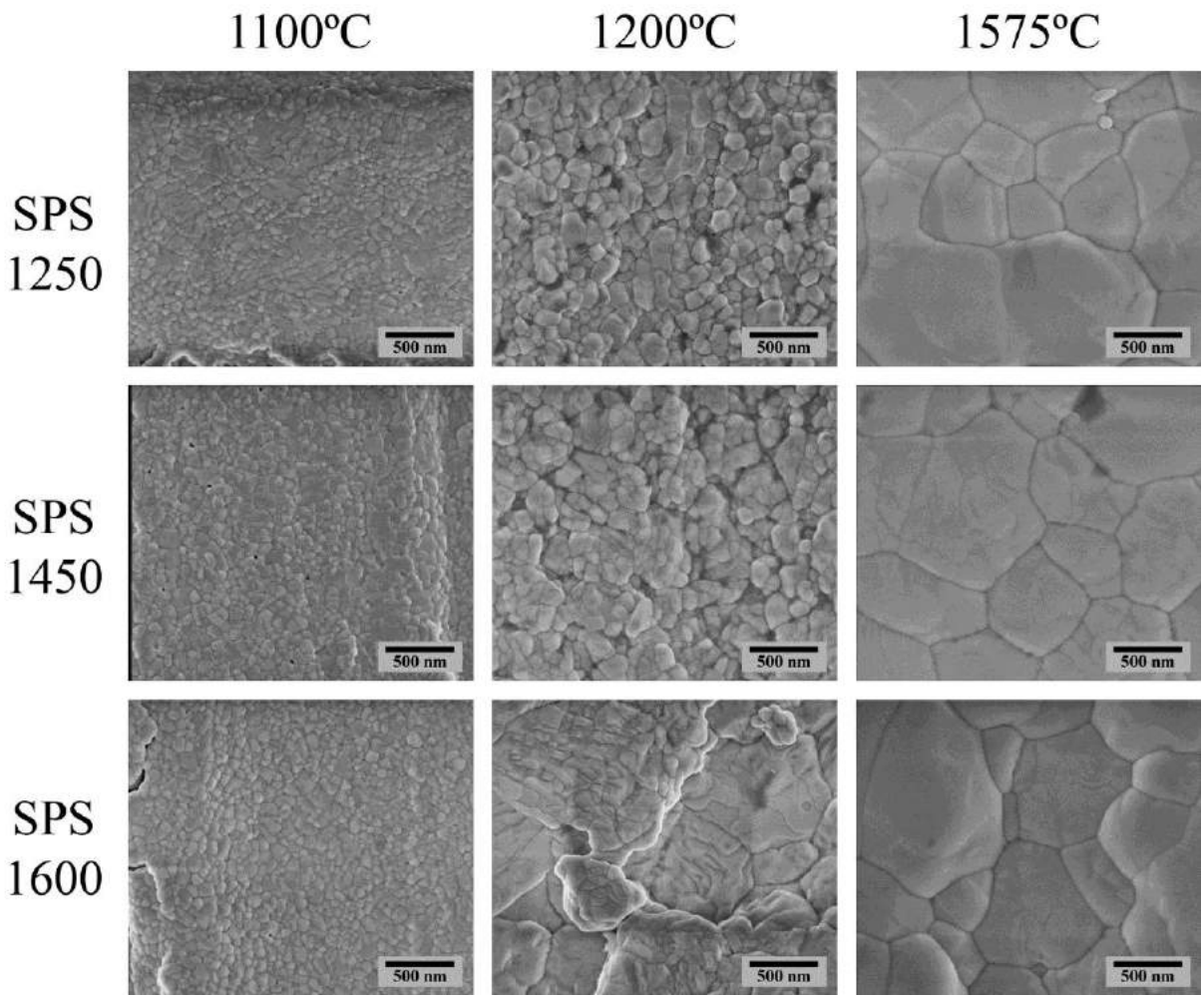

Fig. 3 *Grain size of ASgr SPS specimens after thermal etching for 1 hour at the temperatures indicated on the top row.*

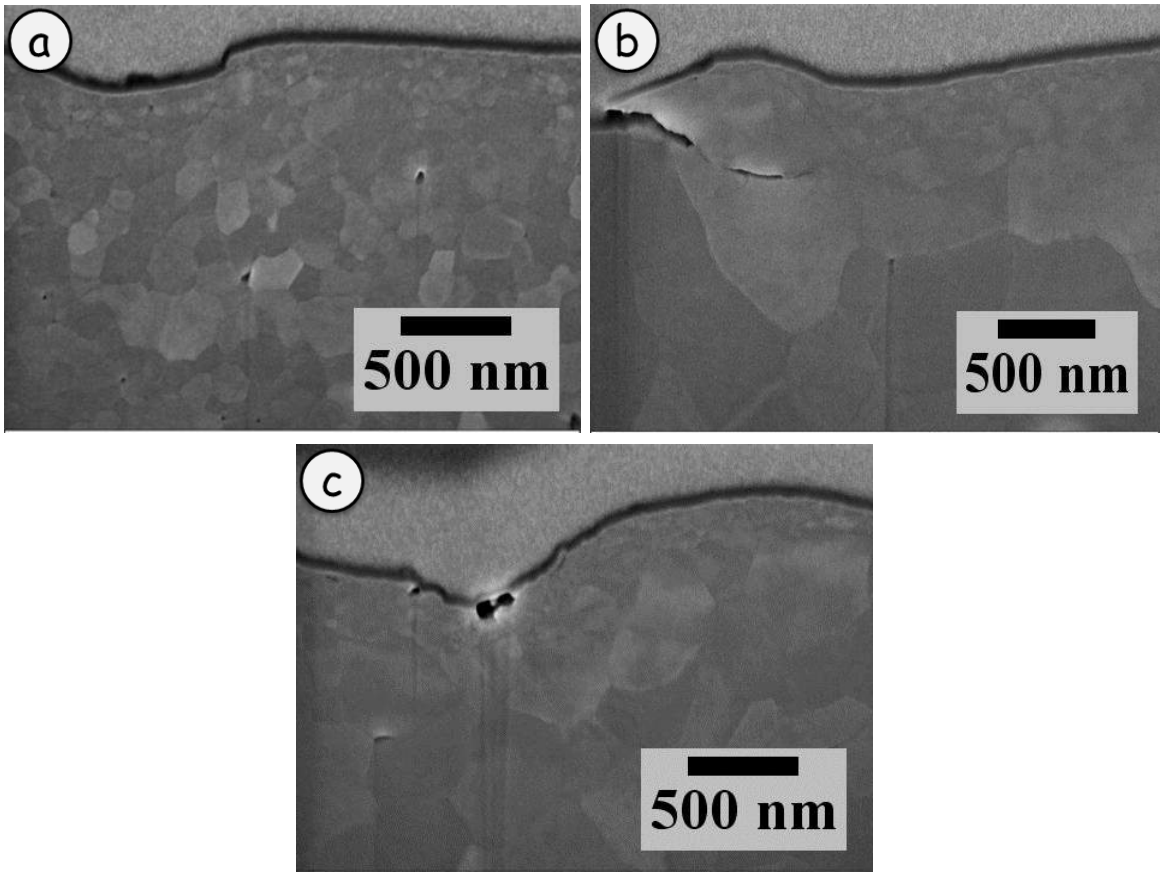

Fig. 4 *Microstructure of ASgr below the surface* ***a)*** *SPS 1250;* ***b)*** *SPS1450 and* ***c)*** *SPS 1600 after grinding and before thermal etching.*

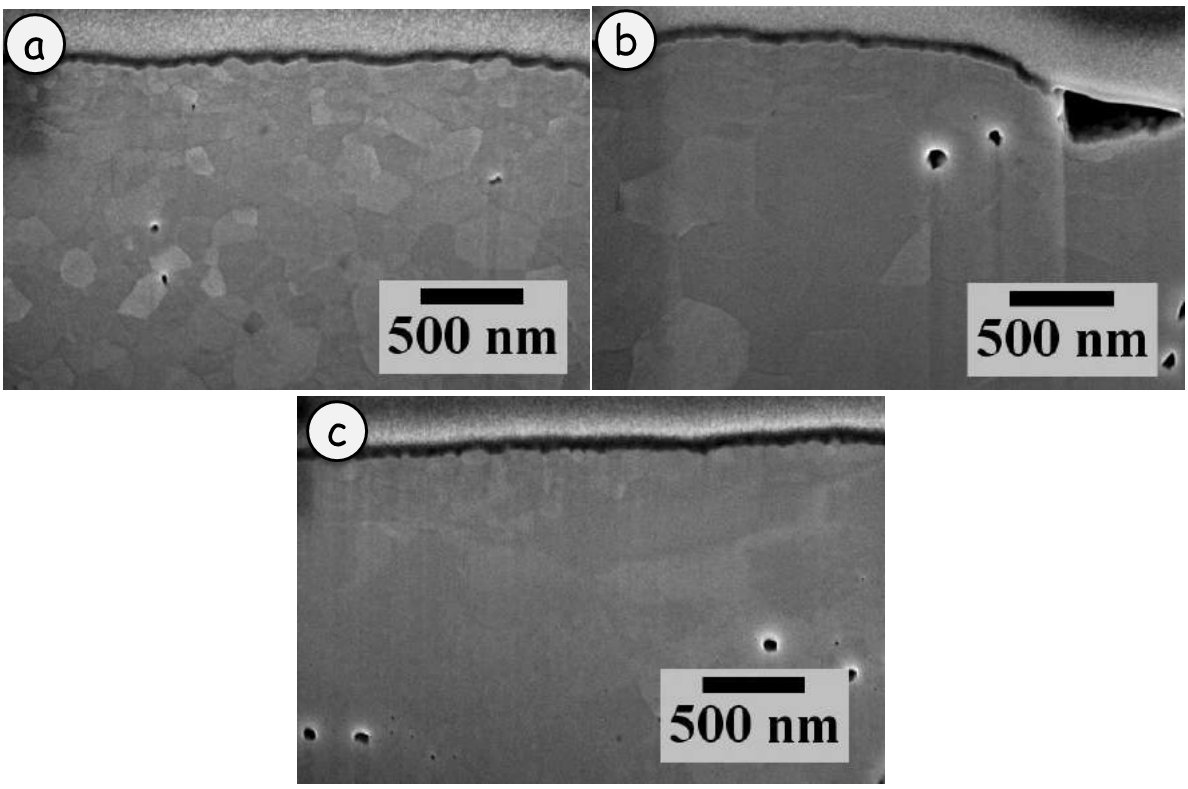

Fig. 5 *Microstructure of ASgr after thermal etching* ***a)*** *SPS 1250 top left;* ***b)*** *SPS1450 top right* ***c)*** *SPS 1600 bottom after grinding and thermal etching.*

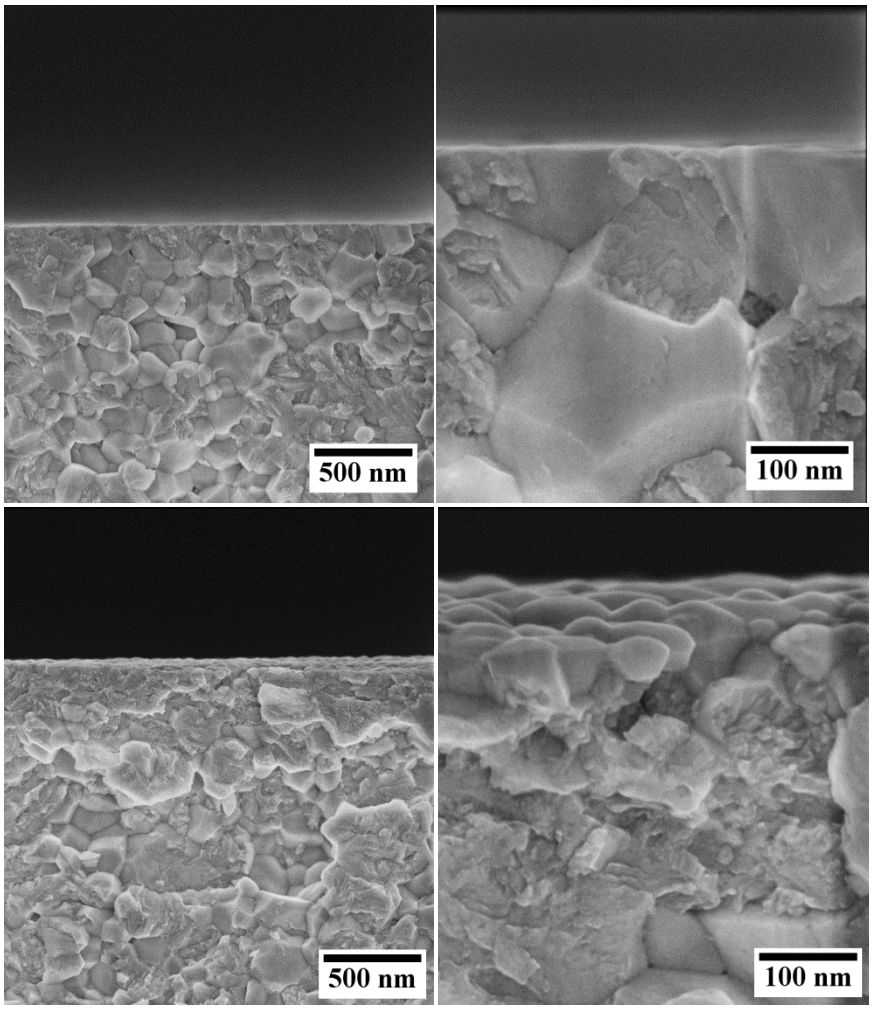

Fig. 6 *Fracture surfaces of ASpol (top) and ASgr (bottom) SPS1250. General views on the left and high magnification details of the surfaces on the right.*

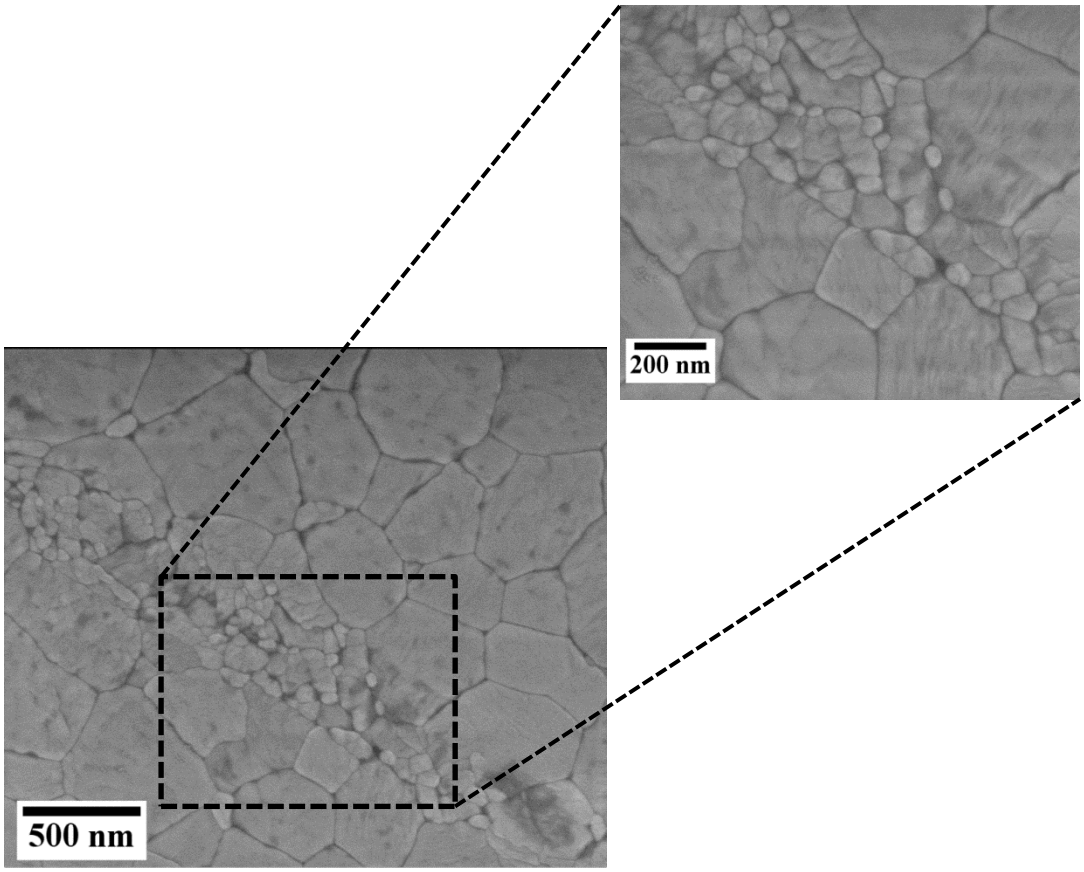

Fig. 7 *Surface of polished SPS 1450 after etching at 1100 °C with the initial grains and the recrystallized grains which appear in scratches still left on the surface after polishing.*